Astrocytic LRRK2 Controls Synaptic Connectivity via Regulation of ERM Phosphorylation

Shiyi Wang[1,9], Ryan Baumert[1,9], Gabrielle Séjourné[1,9], Dhanesh Sivadasan Bindu[1,2], Kylie Dimond[3], Kristina Sakers[1,13], Leslie Vazquez[1,4,9], Jessica Moore[1,13], Christabel Xin Tan[5], Tetsuya Takano[6,7], Maria Pia Rodriguez[1], Scott H. Soderling[1,8,9], Albert R. La Spada[10,11,12], and Cagla Eroglu[1,8,9,13]

[1]The Department of Cell Biology, Duke University Medical Center, Durham, NC, USA

[2]Department of Neonatology, Children's Mercy Hospital, Kansas City, MO, USA

[3]College of Psychology, Nova Southeastern University, Fort Lauderdale, FL, USA

[4]The Department of Neurobiology, Duke University Medical Center, Durham, NC, USA

[5]Life Sciences Institute, University of Michigan, Ann Arbor, MI, USA

[6]Division of Molecular Systems for Brain Function, Kyushu University Institute for Advanced Study, Medical Institute of Bioregulation, Japan

[7]Japan Science and Technology Agency, PRESTO, Japan

[8]The Department of Neurobiology, Duke University Medical Center, Durham, NC, USA

[9]Aligning Science Across Parkinson's (ASAP) Collaborative Research Network, Chevy Chase, MD

[10]The Department of Neurology, Duke University Medical Center, Durham, NC, USA

[11]Departments of Pathology & Laboratory Medicine, Neurology, Biological Chemistry, and Neurobiology & Behavior, University of California, Irvine, CA, USA

[12]UCI Center for Neurotherapeutics, University of California, Irvine, CA, USA

[13]Howard Hughes Medical Institute, Duke University Medical Center, Durham, NC, USA

Corresponding authors: Shiyi Wang: shiyi.wang@duke.edu;

Albert R. La Spada: alaspada@uci.edu;

Cagla Eroglu: cagla.eroglu@duke.edu

SUMMARY

Astrocytes, a major glial cell type of the brain, regulate synapse numbers and function. However, whether astrocyte dysfunction can cause synaptic pathologies in neurological disorders such as Parkinson's Disease (PD) is unknown. Here, we investigated the impact of the most common PD-linked mutation in the leucine-rich repeat kinase 2 (*LRRK2*) gene (G2019S) on the synaptic functions of astrocytes. We found that both in human and mouse cortex, the LRRK2 G2019S mutation causes astrocyte morphology deficits and enhances the phosphorylation of the ERM proteins (Ezrin, Radixin, and Moesin), which are important components of perisynaptic astrocyte processes. Reducing ERM phosphorylation in LRRK2 G2019S mouse astrocytes restored astrocyte morphology and corrected excitatory synaptic deficits. Using an *in vivo* BioID proteomic approach, we found Ezrin, the most abundant astrocytic ERM protein, interacts with the Autophagy-Related 7 (Atg7), a master regulator of catabolic processes. The Ezrin/Atg7 interaction is inhibited by Ezrin phosphorylation, thus diminished in the LRRK2 G2019S astrocytes. Importantly, Atg7 function is required to maintain proper astrocyte morphology. These studies reveal an astrocytic molecular mechanism that could serve as a therapeutic target in PD.

45 **INTRODUCTION**

46 Parkinson's Disease (PD) is a progressive neurodegenerative motor disorder
47 affecting over 8 million people worldwide[1]. PD is commonly diagnosed at the onset of
48 motor symptoms, including tremors, bradykinesia, and rigidity[1]. By the time these motor
49 symptoms are apparent, PD patients have already lost many of their dopaminergic
50 neurons in the substantia nigra pars compacta (SNPc)[2]. However, decades before the
51 onset of motor dysfunction, individuals with PD often display non-motor "prodromal"
52 symptoms, such as cognitive, mood, and sleep disorders, suggesting that early synaptic
53 circuit dysfunction exists across multiple brain regions, including the cerebral cortex[3,4].
54 Even though most PD cases are idiopathic, ~15% are caused by mutations in
55 Parkinsonism genes[5]. The PD-linked genes identified to date point to dysfunction in
56 fundamental cellular processes such as lysosome and mitochondria function, vesicular
57 trafficking, and secretion[6]. However, how the dysfunction of these genes results in
58 impaired synaptic circuits and dopaminergic neuron death is unknown. Moreover, many
59 cell types in the brain and body express these PD-linked genes[7]. Thus, the cellular origins
60 of PD may not be restricted to neurons.

61 Astrocytes instruct the formation and function of synaptic circuits[8,9]. Most synapses
62 in the central nervous system are in direct contact with perisynaptic astrocyte processes
63 (PAPs)[10]. This structural association is essential for regulating synaptic function; therefore,
64 the PAPs and the presynaptic and postsynaptic neuronal compartments are collectively
65 termed "the tripartite synapse"[10]. At the tripartite synapse, astrocytes clear excess
66 neurotransmitters, maintain ion homeostasis, and secrete factors regulating synapse
67 development and function[11]. To accomplish these crucial roles at the synapse, astrocytes

68 gain a highly elaborate morphology and form a network coupled through gap junctions to
69 continuously tile the entire brain parenchyma[8,12,13]. Previous studies found that astrocyte
70 morphogenesis, tiling, and neuronal synaptogenesis are interdependent processes
71 controlled by bidirectional signaling via secreted factors and cell adhesion molecules[14,15].
72 Recent studies also found that astrocytes become reactive, undergoing morphological
73 and molecular changes in numerous neurological disorders, including PD[16,17].

74 Mutations in the leucine-rich repeat kinase 2 (*LRRK2*) gene cause familial PD.
75 Lrrk2 is a large multidomain protein containing ROC (Ras of complex), COR (C-terminal
76 of ROC), catalytic kinase, and four protein-protein interactions domains (armadillo,
77 ankyrin, leucine-rich repeats, WD40 domains)[18,19,]. Lrrk2 plays critical roles in ciliogenesis,
78 lysosome function, immune system, and synaptic vesicle trafficking by phosphorylation
79 of its substrates[20-26]. LRRK2 G2019S is the most common mutation that causes familial
80 PD[20,27,28]. Long before the death of dopaminergic neurons, PD patients with the G2019S
81 mutation have non-motor symptoms, such as depression, hallucinations, and sleep and
82 cognitive disorders[29]. Several rodent models with LRRK2 G2019S mutation do not show
83 motor dysfunction or dopaminergic neuron loss[30,31] but alterations in cortical and cortico-
84 striatal circuits and cognitive problems such as impaired goal-directed actions have been
85 observed[32-34].

86 It is widely accepted that neuronal dysfunction drives synaptic pathologies in PD;
87 however, given the important roles of astrocytes in synaptic connectivity, we reasoned
88 astrocytic dysfunction caused by LRRK2 G2019S mutations can also underlie the circuit
89 phenotypes. Here, we explored this possibility by using LRRK2 G2019S knockin ($^{ki/ki}$)

90 mouse model[35,36] in conjunction with *in vivo* astrocyte-specific genetic, proteomic,
91 electrophysiological, and biochemical approaches.

92 **RESULTS**

93 **LRRK2 G2019S mutation causes ERM hyperphosphorylation in the prefrontal**
94 **cortices of mice and humans.**

95 Cortical astrocytes play critical roles in cognitive functions by controlling the
96 number and activity of synapses. Their highly elaborate morphology allows them to
97 physically and functionally interact with thousands of synapses through their PAPs[37,38].
98 In disease states, astrocytes change their morphology and tiling, which is proposed to
99 induce synaptic abnormalities[39].

100 To study how the LRRK2 G2019S mutation impacts astrocytes in the prefrontal
101 cortex, a cortical region linked to PD, we stained sections from the frontal cortices of age
102 and sex-matched control and LRRK2 G2019S mutation-carrying PD patients
103 (Supplemental Table 1) with glial fibrillary acidic protein (GFAP, a marker for astrocyte
104 branches) and phosphorylated ERM (Phospho-ERM, which are enriched in PAPs) (Figure
105 1A). Remarkably, the astrocytic organization, determined by GFAP staining, was severely
106 disrupted, and GFAP levels were significantly elevated (~42%) in PD patients carrying
107 the LRRK2 G2019S mutation, indicative of reactive gliosis (Figure 1B-C). Unexpectedly,
108 the phospho-ERM signal was increased by 7-fold in the frontal cortices of PD patients
109 carrying the LRRK2 G2019S mutation (Figure 1B-C). The elevated phospho-ERM signal
110 was observed in GFAP-positive astrocytes and other cortical cells. These data reveal that

111 there are reactive astrocytes in the cortices of LRRK2 G2019S PD patients, and ERM
112 phosphorylation is highly upregulated in the brains of these patients.

113 Is ERM hyperphosphorylation an early or late event in LRRK2 G2019S PD
114 pathology? To address this question, we utilized the LRRK2 G2019S$^{ki/ki}$ mice in which the
115 human G2019S point mutation was introduced into exon 41 of the mouse *Lrrk2* gene[35,36].
116 To determine if ERM hyperphosphorylation localizes to astrocytes, we crossed these
117 mice to an astrocyte reporter line carrying the Aldh1L1-eGFP transgene, which labels all
118 astrocytes by GFP[40]. We examined the levels of phospho-ERM in coronal brain sections
119 from 21-day-old (P21, juvenile) and 12-week-old (P84, adult) WT or LRRK2 G2019S$^{ki/ki}$
120 mice. In LRRK2 G2019S$^{ki/ki}$ mice, a brain region-specific and heterogeneous increase in
121 phospho-ERM staining was observed in astrocytes across both age groups, compared to
122 WT mice (Figure 1D-L). The increase in phospho-ERM in LRRK2 G2019S$^{ki/ki}$ mice was
123 localized to a subpopulation of astrocytes within layers (L)1 and L2-3 of the anterior
124 cingulate cortex (ACC) and the primary motor cortex (MOp) (Figure 1E-L; Figure S1A-C)
125 but was absent in other regions such as the primary sensory cortex (SSp) and the dorsal
126 medial striatum (DMS) (Figure S1D-I). In P21 LRRK2 G2019S$^{ki/ki}$ mice, the phospho-ERM
127 integrated densities in the ACC and MOp L1 and L2-3 were increased by ~32% (ACC)
128 and ~41% (MOp) compared to the WTs (Figure 1I), whereas in P84 LRRK2 G2019S$^{ki/ki}$
129 mice, the phospho-ERM integrated densities were increased by ~57% (ACC) and ~37%
130 (MOp) compared to the WTs (Figure 1L). Importantly, we did not observe any difference
131 in total ERM levels in the ACC and MOp between WT and LRRK2 G2019S$^{ki/ki}$ brain
132 sections (Figure S1J-L). These findings show that the LRRK2 G2019S mutation

133 enhanced ERM phosphorylation in cortical astrocytes *in vivo*. This increase in ERM
134 phosphorylation is not uniform but rather localized to a subset of ACC and MOp astrocytes.

135 These findings reveal that the LRRK2 G2019S mutation increases phospho-ERM
136 levels in the cortices of PD patients and mice. In the human samples, phospho-ERM
137 elevation was observed concurrently with reactive gliosis (elevated GFAP staining). To
138 determine if, in LRRK2 G2019S$^{ki/ki}$ mice, there were reactive astrocytes detectable at
139 early ages, we stained sections from the same P21 mouse brains with an anti-GFAP
140 antibody. In the mouse cortex, grey matter astrocytes do not display GFAP staining
141 unless there is reactive gliosis[41,42]. We did not detect any increase in the levels of GFAP
142 (Figure S2A-C), indicating that phospho-ERM upregulation does not occur concurrently
143 with reactive astrogliosis in LRRK2 G2019S$^{ki/ki}$ mice. Distinct from the P21 and P84
144 LRRK2 G2019S$^{ki/ki}$ mice where phospho-ERM was restricted to a subset of astrocytes in
145 a brain region-specific manner, in the human patient brains (~80 years old), we saw
146 phospho-ERM accumulation outside the GFAP-labelled astrocytes. This observation
147 suggests aberrant ERM hyperphosphorylation in multiple cell types occurs at later stages
148 of PD in patients with LRRK2 G2019S mutation.

149 **LRRK2 G2019S mutation alters excitatory and inhibitory synapse numbers and**
150 **function in the cortex.**

151 Previous studies did not observe dopaminergic neuron loss or motor dysfunction
152 in the LRRK2 G2019S$^{ki/ki}$ mice[31,43]; however, synapse dysfunction at cortico-striatal
153 circuits was reported in adult mice[34]. Despite the critical role of Lrrk2 in cortico-striatal
154 synapses and PD-related cortical circuits[44], whether LRRK2 G2019S affects cortical

155 synapse numbers and function has not been explored. Understanding these cortical
156 synaptic abnormalities is crucial, as they may underlie the early cognitive deficits in PD
157 that are unrelated to dopaminergic dysfunction. Therefore, we next investigated how
158 LRRK2 G2019S mutation impacts synaptic connectivity in the ACC and MOp L1 and L2-
159 3 (Figure 2A), regions in which ERM hyperphosphorylation within astrocytes was
160 observed.

161 Astrocytes, through secreted factors and direct contact with synapses, strongly
162 promote excitatory and inhibitory synapse formation and maintenance[13]. We quantified
163 the density of structural excitatory and inhibitory intracortical synapses in WT and LRRK2
164 G2019S$^{ki/ki}$ mice. To do so, we marked the excitatory synapses as the co-localization of
165 the presynaptic Vesicular Glutamate Transporter 1 (VGlut1) and the Postsynaptic Density
166 Protein (PSD95), whereas inhibitory synapses were labeled using presynaptic Vesicular
167 GABA Transporter (VGAT), and postsynaptic gephyrin (GEPHYRIN)[45,46] (Figure 2B).
168 Structural synapses were identified as the apposition and co-localization of presynaptic
169 and postsynaptic markers, which are in two distinct neuronal compartments (i.e., axons
170 and dendrites) and would only appear to co-localize at synapses due to their proximity[47].

171 Excitatory synapse densities were quantified both at P21 and P84. In the ACC of
172 the LRRK2 G2019S$^{ki/ki}$ mice, there was a significant decrease in intracortical excitatory
173 synapse densities in both layers and ages we analyzed (~30%) when compared to the
174 WT controls (Figure 2C-D and Figure S3A-B). However, no differences in excitatory
175 synapse numbers were observed between genotypes in the MOp (Figure 2E-F and Figure
176 S3C-D). When we quantified the densities of inhibitory synapses in the MOp, we found
177 significant differences between genotypes (~40% increase). In contrast, no differences

178 were observed for inhibitory synapse numbers in the ACC of WT and LRRK2 G2019S$^{ki/ki}$
179 mice (Figure 2G-J). These results revealed that the LRRK2 G2019S mutation causes a
180 brain region-specific reduction in excitatory synapse densities in the ACC and an increase
181 in inhibitory synapse densities in the MOp, highlighting brain region-specific synaptic
182 alterations associated with this mutation.

183 Next, we used electrophysiology to test the functional impact of altered synapse
184 density in the ACC and the MOp of LRRK2 G2019S$^{ki/ki}$ mice on synaptic function. We
185 recorded miniature excitatory postsynaptic currents (mEPSCs) in the ACC L2-3 pyramidal
186 neurons and miniature inhibitory postsynaptic currents (mIPSCs) in the MOp L2-3
187 pyramidal neurons from acute brain slices of P84 LRRK2 G2019S$^{ki/ki}$ and WT mice. In
188 agreement with a reduction in excitatory synapse density in the ACC, LRRK2 G2019S$^{ki/ki}$
189 L2-3 neurons displayed mEPSC frequency reduced by ~65% and a corresponding right
190 shift in the cumulative distributions of mEPSC inter-event intervals (Figure 3A-B) when
191 compared to WT neurons. There were no significant changes in the mean mEPSC
192 amplitude between genotypes (Figure 3C). mEPSC frequency changes correlate with
193 synapse numbers and/or the probability of presynaptic glutamate release[48], whereas
194 mEPSC amplitude indicates the synaptic strength reflecting the number of AMPARs at
195 the postsynapse[49]. Therefore, together with our anatomical data, these physiological
196 analyses reveal that the LRRK2 G2019S mutation reduces the number of intracortical
197 excitatory connections formed on L2-3 pyramidal neurons in the ACC without a change
198 in synaptic strength. In contrast, in the MOp, we found a robust ~72% increase in mIPSC
199 frequency when we recorded from the L2-3 pyramidal neurons of the LRRK2 G2019S$^{ki/ki}$
200 mice compared to WT, with no significant change in amplitude (Figure 3D-F). The

201 increased mIPSC frequency aligns with our findings that inhibitory synapse numbers are
202 elevated in the MOp of the LRRK2 G2019S$^{ki/ki}$ mice.

203 **Reducing ERM hyperphosphorylation in astrocytes rescues excitatory synapse**
204 **density and function in the ACC of adult LRRK2 G2019S$^{ki/ki}$ mice.**

205 Lrrk2 phosphorylates a conserved threonine residue present in all ERM
206 proteins[50,51]. We found that LRRK2 G2019S mutation leads to increased ERM
207 phosphorylation in astrocytes (Figure 1). We hypothesized that dampening ERM
208 phosphorylation, specifically in astrocytes, might be sufficient to restore the synapse
209 alteration in LRRK2 G2019S$^{ki/ki}$ mice. To test this hypothesis specifically in astrocytes *in*
210 *vivo*, we first investigated if we could reduce ERM phosphorylation in LRRK2 G2019S$^{ki/ki}$
211 astrocytes by virally overexpressing an Ezrin mutant lacking the ability to be
212 phosphorylated. We chose Ezrin because Ezrin is highly abundant and specifically
213 enriched in astrocytes compared to its family members, Radixin and Moesin[52] (Figure
214 S4A-B). Switching the amino acid threonine (T) at location 567 with alanine (A) results in
215 a version of the protein that cannot be phosphorylated (Phospho-dead Ezrin, Figure
216 S4C)[53,54].

217 To determine if phospho-dead Ezrin can reduce ERM phosphorylation in
218 astrocytes of LRRK2 G2019S$^{ki/ki}$ mice, we retro-orbitally injected 9-week-old WT and
219 LRRK2 G2019S$^{ki/ki}$ mice with adenoviruses (AAVs) to express Hemagglutinin (HA)-
220 tagged WT Ezrin or phospho-dead Ezrin under the control of the astrocyte-specific
221 GfaABC1D promoter (Figure S4D). The injected mouse brains were harvested at 12
222 weeks (3 weeks after injection) for histological analyses.

223 The widespread viral expression of Ezrin in astrocytes was verified by staining with
224 an anti-HA tag antibody (Figure 4A). First, overexpressing WT or phospho-dead Ezrin in
225 WT mouse brains did not increase the phospho-ERM level in the ACC and MOp (Figure
226 4A-B). However, WT Ezrin overexpression in the LRRK2 G2019S$^{ki/ki}$ mouse brains was
227 accompanied by a robust phospho-ERM elevation in a population of astrocytes in the
228 ACC and MOp (Figure 4A-B). In contrast, overexpression of the phospho-dead Ezrin
229 eliminated the ERM hyperphosphorylation in the LRRK2 G2019S$^{ki/ki}$ ACC and MOp
230 (Figure 4A-B). This observation indicates that the LRRK2 G2019S mutation sensitizes
231 astrocytes to Lrrk2-mediated ERM phosphorylation.

232 To determine if overexpressing phospho-dead Ezrin can also dampen
233 hyperphosphorylation of another Lrrk2 substrate, Rab10[27,55], We stained sections from
234 the same brains as in Figure 4A-B with antibodies against phosphorylated Rab10 (Thr
235 73). Rab10 is a member of the Rab family of small GTPases that plays crucial roles in
236 neuronal function and intracellular transport pathways[56]. As expected, we found higher
237 Rab10 phosphorylation in LRRK2 G2019S$^{ki/ki}$ brain sections than in WT mice. However,
238 neither WT nor phospho-dead Ezrin overexpression impacted Rab10 phosphorylation
239 (Figure S5A-B). These results show that phospho-dead Ezrin overexpression in
240 astrocytes specifically reduces ERM hyperphosphorylation without impacting another
241 Lrrk2 substrate, Rab10.

242 Given the effects of phospho-dead Ezrin in dampening ERM hyperphosphorylation,
243 we next tested whether this manipulation in adult LRRK2 G2019S$^{ki/ki}$ astrocytes can
244 reverse the synaptic phenotypes we observed in the ACC and MOp. To do so, we
245 followed the same experimental strategy and timeline as in Figure S4D. WT Ezrin

246 overexpression in astrocytes did not affect the excitatory synapse density decline in the
247 ACC L1 and L2-3 of LRRK2 G2019S$^{ki/ki}$ mice. In contrast, overexpression of phospho-
248 dead Ezrin reduced excitatory synapse density in the WT background by ~30% (Figure
249 4C-D). Conversely, astrocytic overexpression of phospho-dead Ezrin in LRRK2
250 G2019S$^{ki/ki}$ rescued the excitatory synapse numbers to WT levels in the ACC (Figure 4C-
251 D). These data suggest that the reduction in synapse numbers we observed in the ACC
252 of the LRRK2 G2019S$^{ki/ki}$ mice is largely due to an astrocytic dysfunction through
253 dysregulated ERM phosphorylation. These results also indicate that astrocytes contribute
254 to excitatory synaptic dysfunction in the LRRK2 G2019S$^{ki/ki}$ mouse cortex.

255 We next investigated whether the same manipulation of adult astrocytes can
256 change the inhibitory synapse number in the MOp. We found that neither the WT nor the
257 phospho-dead Ezrin overexpression in adult astrocytes can rescue the density of
258 inhibitory synapses back to WT levels in the MOp L1 and L2-3 of LRRK2 G2019S$^{ki/ki}$ mice
259 (Figure S5C-D). In summary, phospho-dead Ezrin expression in adult WT or LRRK2
260 G2019S$^{ki/ki}$ astrocytes is sufficient to modify excitatory synapse numbers in the ACC but
261 cannot restore or impair inhibitory synaptic connectivity in the MOp. It is plausible that
262 LRRK2 G2019S mutation impairs inhibitory synapses in the MOp by altering the number
263 or connectivity of cortical interneurons through a developmental mechanism. Thus,
264 manipulation in adults is insufficient to eliminate this inhibitory synapse phenotype.

265 Because astrocytic overexpression of phospho-dead Ezrin impacted excitatory
266 synapse numbers in the ACC of WT and LRRK2 G2019S$^{ki/ki}$ mice, we next performed
267 whole-cell patch-clamp recordings from ACC L2-3 pyramidal neurons transduced with the
268 same AAVs. Overexpression of WT Ezrin in LRRK2 G2019S$^{ki/ki}$ astrocytes did not rescue

269 the decreased frequency of mEPSCs in ACC L2-3 neurons. However, overexpression of
270 phospho-dead Ezrin in LRRK2 G2019S$^{ki/ki}$ astrocytes restored the frequency up to the
271 levels of WT mice expressing WT Ezrin (Figure 4E-F). Interestingly, overexpression of
272 phospho-dead Ezrin in WT astrocytes significantly reduced the frequency of mEPSCs
273 (~54%) in WT ACC neurons (Figure 4E-F). Posthoc comparisons confirmed no significant
274 differences in mean mEPSC amplitudes across all 4 conditions (Figure 4G).

275 Altogether, these electrophysiological and neuroanatomical analyses show that
276 the LRRK2 G2019S mutation reduces the density and function of excitatory synaptic
277 inputs made onto the ACC L2-3 but increases the density and function of inhibitory
278 synaptic inputs made onto the MOp L2-3. These data reveal that the LRRK2 G2019S
279 mutation dysregulates proper excitatory and inhibitory synapse connectivity and function
280 in the cortex in a brain region-specific manner. Because astrocytes control the number
281 and function of cortical synapses, these results also pinpoint a link between LRRK2
282 G2019S-mediated ERM hyperphosphorylation in astrocytes (Figure 1) and the synaptic
283 dysfunctions in the ACC and MOp (Figure 2 and 3). Our results also reveal that astrocytic
284 overexpression of phospho-dead Ezrin in adult LRRK2 G2019S$^{ki/ki}$ mice can recover
285 excitatory synapse density and function, whereas the same manipulation disrupts
286 synapse numbers and function in WT ACC neurons (Figure 4). These findings show that
287 balancing ERM phosphorylation in astrocytes is crucial for maintaining excitatory synapse
288 density and function in the ACC.

289 **Lrrk2 regulates astrocyte morphological complexity *in vivo* through ERM**
290 **phosphorylation.**

291 Astrocytes gain their elaborate morphology during the second and third postnatal
292 weeks in mice[57,58]. Previous studies highlighted the importance of astrocyte morphology
293 in the regulation of synapse numbers and function[13]. ERM proteins are structural
294 components of perisynaptic astrocyte processes[59]. When phosphorylated and bound to
295 phosphatidylinositol 4,5-bisphosphate (PIP2), ERM proteins change conformation and
296 link the F-actin cytoskeleton to the cell membrane[54]. This switch is thought to be important
297 in organizing cell morphology by allowing process outgrowth[53,54]. Ezrin is the most
298 abundant ERM protein in astrocytes and is required for proper astrocyte
299 morphogenesis[60-62]. Based on our observation that ERM hyperphosphorylation in LRRK2
300 G2019S$^{ki/ki}$ astrocytes causes aberrant cortical synaptic connectivity as early as P21, we
301 next investigated how this mutation impacts astrocyte morphological complexity.

302 To determine if astrocyte morphology was altered in the LRRK2 G2019S$^{ki/ki}$
303 cortices, we sparsely labeled astrocytes with a membrane-targeted fluorescent protein
304 (mCherry-CAAX), using postnatal astrocyte labeling by electroporation (PALE) in WT and
305 LRRK2 G2019S$^{ki/ki}$ mice and imaged whole astrocytes with confocal microscopy at high
306 resolution (Figure S6A). We focused our analyses of astrocyte territory size and
307 complexity (see Methods for details) on the ACC and MOp L1 and L2-3 at P21. In LRRK2
308 G2019S$^{ki/ki}$ mice, the territory volumes of astrocytes were significantly smaller (reduced
309 by ~34%) than WT astrocytes (Figure 5A-B). In addition, compared to WT astrocytes,
310 LRRK2 G2019S$^{ki/ki}$ astrocytes were significantly less complex (Figure 5C). But the
311 reduction in astrocyte size and complexity in LRRK2 G2019S$^{ki/ki}$ did not change the
312 number of ALDH1L1+/SOX9+ cells in the ACC and MOp (Figure S6B-D). These results

313 reveal that LRRK2 G2019S mutation reduces astrocyte morphological complexity without
314 affecting astrocyte numbers *in vivo*.

315 Because phospho-dead Ezrin overexpression in astrocytes differentially impacts
316 synapse numbers and function in WT and LRRK2 G2019S$^{ki/ki}$ mice (Figure 4), we
317 hypothesized that overexpression of phospho-dead Ezrin would also impact astrocyte
318 morphology differently between genotypes. To test this possibility, we performed PALE
319 to introduce mCherry-CAAX and phospho-dead Ezrin into WT or LRRK2 G2019S$^{ki/ki}$
320 mouse astrocytes. The overexpression of phospho-dead Ezrin decreased the territory
321 volume and morphological complexity of WT astrocytes (Figure 5A-C). However,
322 phospho-dead Ezrin expression restored astrocyte territory volume and complexity in
323 LRRK2 G2019S$^{ki/ki}$ mice (Figure 5A-C). Our results show that the abundance of
324 unphosphorylated Ezrin differentially regulates astrocyte morphology in WT versus
325 LRRK2 G2019S$^{ki/ki}$ astrocytes.

326 Previous studies suggested phosphorylation at T567 promotes Ezrin acquiring an
327 open conformation by binding to phosphatidylinositol-4,5-bisphosphate (PIP2)[63]. In this
328 conformation, the N-terminus interacts with membrane proteins, and the C-terminus is
329 available to bind to the actin cytoskeleton[64,65]. An Ezrin mutant in which the T567 residue
330 is switched with aspartate (D) prefers Ezrin's open conformation, thereby mimicking the
331 phosphorylated state (Phospho-mimetic Ezrin, Figure S4C)[66,67]. Conversely, the
332 phospho-dead Ezrin remains in the closed conformation in which the N and C terminal
333 domains are bound together. This closed conformation is proposed to be unable to
334 interact with membranes or actin[53,68]. Because we found that phospho-dead Ezrin
335 differentially impacts WT and LRRK2 G2019S$^{ki/ki}$ astrocytes, we hypothesized that Ezrin's

336 transition between open and closed conformation is regulated by LRRK2 function and
337 should be tightly balanced for proper astrocyte morphogenesis (Figure 5D). In LRRK2
338 G2019S$^{ki/ki}$ astrocytes, Ezrin is more likely to be phosphorylated and in the open state.
339 This distorted balance of the Ezrin state may explain the morphological defects of LRRK2
340 G2019S$^{ki/ki}$ astrocytes. This model also aligns with our findings that dampening Ezrin
341 phosphorylation via phospho-dead Ezrin disrupts WT astrocyte morphology but rescues
342 the deficits in LRRK2 G2019S$^{ki/ki}$ astrocytes.

343 If this model is correct, we would expect that the loss of Lrrk2 function in astrocytes
344 impacts astrocyte morphogenesis, a phenotype that we could rescue by introducing
345 phospho-mimetic Ezrin. To test the impact of Lrrk2 loss in astrocytes, first, we used a
346 knockout (KO)-verified Lrrk2 antibody[69,70] and confirmed the expression of Lrrk2 protein
347 in cortical mouse astrocytes by immunostaining coronal brain sections from WT or LRRK2
348 G2019S$^{ki/ki}$ mice. Lrrk2 staining was evident in WT and LRRK2 G2019S$^{ki/ki}$ astrocytes,
349 localizing throughout astrocytic processes (Figure S7A-B). In addition, cortical astrocytes
350 isolated from WT rats express Lrrk2 *in vitro,* which was detected by immunoblotting
351 (Figure S7C-D). In agreement, RNA sequencing databases for cortical cell types in mice
352 and humans also show *lrrk2* mRNA present in astrocytes (Fig. S7C-D).

353 To test if astrocytic Lrrk2 function is required to control astrocyte morphogenesis,
354 we knocked down Lrrk2 in WT astrocytes *in vivo*, using PALE. We transfected astrocytes
355 with the mCherry-CAAX reporter and either with a control shRNA (shControl) or a shRNA
356 that reduces Lrrk2 expression by ~90% (Figure S7E-F, targets both rat and mouse Lrrk2).
357 Interestingly, similar to LRRK2 G2019S$^{ki/ki}$ astrocytes, shLrrk2- transfected astrocytes had

358 significantly smaller territory volumes (reduced by ~36%) and reduced morphological
359 complexity when compared to shControl astrocytes (Figure 5E-G).

360 Could phospho-mimetic Ezrin rescue the morphological complexity of shLrrk2-
361 transfected astrocytes? To test this, we performed PALE to introduce shLrrk2 or
362 shControl with a phospho-mimetic Ezrin overexpression vector. Overexpression of
363 phospho-mimetic Ezrin in shControl astrocytes did not change astrocyte territory volume
364 and morphological complexity compared to only shControl-transfected astrocytes (Figure
365 5E-G). However, expression of phospho-mimetic Ezrin in shLrrk2-containing astrocytes
366 restored astrocyte territory volume and morphological complexity up to the levels of
367 shControl-transfected astrocytes (Figure 5E-G).

368 These results show that both the gain of Lrrk2 kinase function (in LRRK2
369 G2019S$^{ki/ki}$ mice) and the loss of Lrrk2 function (shLrrk2) decreases astrocyte complexity
370 and size. In line with our model, we found that the opposite manipulation of Ezrin
371 conformational/phosphorylation states can rescue these morphological phenotypes.
372 Interestingly, in the shControl astrocytes overexpressed with phospho-mimetic Ezrin, we
373 did not observe a reduction in astrocyte territory and morphological complexity. This
374 outcome can be explained by the presence of endogenous Ezrin in its closed
375 conformation, which balances the additional phospho-mimetic Ezrin. These findings
376 reveal that Lrrk2 is crucial to regulate astrocyte morphological complexity via balancing
377 ERM phosphorylation *in vivo*.

378 **LRRK2 G2019S mutation interrupts Ezrin interactomes in astrocytes**

379 What are the molecular mechanisms by which ERM hyperphosphorylation stunts
380 astrocyte morphology in LRRK2 G2019S$^{ki/ki}$ astrocytes? To address this question, we
381 identified possible interactors of Ezrin in WT and LRRK2 G2019S$^{ki/ki}$ astrocytes by *in vivo*
382 astrocyte-specific proximity labeling. To do so, we used two virally encoded astrocyte-
383 specific biotin ligase (BirA2) probes: Ezrin fused with BirA2 (Astro-Ezrin-BirA2) and
384 soluble BirA2 with a nuclear export sequence (Astro-Cyto-BirA2) (Figure 6A). The viruses
385 were delivered using intracortical AAV injections to P0-2 WT and LRRK2 G2019S$^{ki/ki}$
386 mouse pups. AAV-injected mice were given subcutaneous biotin injections starting at P18
387 for 3 days, and cortices were collected at P21 (Figure 6B). Biotinylated proteins were
388 detected in astrocytes using immunohistochemistry and immunoblotting for HA and
389 Streptavidin (Figure S8A-C).

390 Biotinylated proteins from cortices were affinity-purified and analyzed using
391 quantitative liquid chromatography-tandem mass spectrometry (LC-MS) (Figure 6B).
392 Across the samples, we identified 30,815 unique peptides corresponding to 4,081 unique
393 proteins. Principle component analyses (PCA) of iBioID results showed that Cyto-BioID
394 (control) and Ezrin-BioID (bait) samples cluster separately, and Ezrin-BioID samples from
395 WT or LRRK2 G2019S$^{ki/ki}$ astrocytes form distinct clusters (Figure S9A). We detected
396 Radixin and Moesin, known Ezrin family proteins, to be significantly enriched in the Ezrin-
397 BioID sample compared to Cyto-BioID (Figure S9B)[71].

398 To delineate genotype-specific interactors of Ezrin, we performed a comparative
399 analysis of putative Ezrin interactors from WT versus LRRK2 G2019S$^{ki/ki}$ mice. Astro-
400 Ezrin-BioID detected 344 proteins at a significantly different abundance (fold-change >
401 1.5 or < -1.5, $p < 0.05$) between genotypes. 190 were found to gain proximity to Ezrin in

402 LRRK2 G2019S$^{ki/ki}$ astrocytes; whereas 154 lost Ezrin proximity (Figure 6C; Figure S9C-
403 D).

404 To determine how changes in the Ezrin interactome may impact molecular
405 processes and cellular functions in astrocytes, we applied Gene Ontology (GO) analysis
406 to the 344 proteins that were differentially enriched between genotypes. We found that
407 terms for molecular functions related to phospholipid binding, microtubule binding, and
408 membrane transporter and cell-adhesion mediator activity were over-represented in
409 differentially enriched proteins (Figure 6D). This aligns with our model that the LRRK2
410 G2019S mutation would shift Ezrin towards its phosphorylated/open state, which is
411 associated with membranes by binding lipids and membrane proteins. Unexpectedly,
412 when we applied GO-term analyses to biological processes, we found terms such as
413 catabolic processes, macroautophagy, negative regulation of developmental growth, and
414 intracellular transport to be overrepresented (Figure 6E). These findings indicated a role
415 for Ezrin in these biological processes, which are altered by the LRRK2 G2019S mutation.

416 Previous studies in neurons and other cell types demonstrated macroautophagy
417 deficits when the LRRK2 G2019S mutation is present[72]. Therefore, we next analyzed
418 global changes in the cytosol induced by the LRRK2 G2019S mutation by comparing the
419 Astro-Cyto-BioID datasets of all astrocytic proteins across genotypes. There were 195
420 proteins that were differentially enriched in the Cyto-BioID depending on the genotype
421 (78 gained and 117 lost in LRRK2 G2019S$^{ki/ki}$, Figure S9E). GO-term analysis of
422 differentially detected cytosolic proteins revealed an enrichment of proteins associated
423 with phospholipid binding and vesicle trafficking (Figure S9F-G). Macroautophagy,
424 catabolic processes, and related GO-terms did not enrich in Cyto-BioID, suggesting that

425 changes in these biological processes that we found in the Ezrin-BioID are specifically
426 related to alterations in Ezrin function in the LRRK2 G2019S$^{ki/ki}$ astrocytes.

427 iBioID captures proteins that are in close proximity to the bait but does not
428 guarantee direct protein-protein interactions. To identify potential direct interactors of
429 Ezrin which are differentially regulated by LRRK2 G2019S mutation, we compared protein
430 abundance in Astro-Ezrin-BioID to Astro-Cyto-BioID within each genotype (Ezrin/Cyto
431 fold -change > 1.5, $p > 0.05$, 346 proteins in WT and 335 proteins in LRRK2 G2019S$^{ki/ki}$).
432 To generate high-confidence lists of interactors that gained or lost proximity to Ezrin in
433 LRRK2 G2019S$^{ki/ki}$ astrocytes, we set a second requirement for proteins with fold-change
434 > 1.5 or < -1.5 between LRRK2 G2019S$^{ki/ki}$ and WT Astro-Ezrin-BioID. Using these filters,
435 we narrowed down our list to 28 as "gained proximity to Ezrin in LRRK2 G2019S
436 astrocytes" and 30 as "lost proximity to Ezrin in LRRK2 G2019S astrocytes" (Figure 6F-
437 H; Supplemental Table 2).

438 Taken together, these data provide a comprehensive map of Ezrin interactomes in
439 WT and LRRK2 G2019S$^{ki/ki}$ mouse astrocytes *in vivo*. This discovery-based approach
440 reveals unexpected changes in Ezrin interactions with proteins that function in catabolic
441 processes and autophagy in the astrocytes of LRRK2 G2019S$^{ki/ki}$ mice. Thus, it points us
442 towards a molecular mechanism underlying the role of Lrrk2-Ezrin signaling pathways in
443 astrocyte morphogenesis.

444 **Atg7 is an Ezrin interactor that is required for proper astrocyte morphogenesis**

445 Among the high-confidence astrocytic Ezrin interactors, we identified autophagy-
446 related gene 7 (Atg7), a crucial autophagy regulator. Atg7 was highly enriched (~2.3-fold)

447 in the Ezrin-BioID fraction of WT astrocytes but was less abundant (-2.0-fold) in the Ezrin-
448 BioID fraction of LRRK2 G2019S$^{ki/ki}$ astrocytes compared to the Cyto-BioID. Atg7
449 encodes an E1-like ubiquitin-activating enzyme and plays a crucial role in the initiation of
450 autophagy[73]. Studies in mice and humans have also pointed to the dysregulation of Atg7
451 in neurological disorders[74]. However, little is known about the role of Atg7 in astrocytes,
452 and whether it can directly interact with Ezrin and regulate astrocyte morphology is
453 unknown.

454 First, to examine the putative interaction between Ezrin and Atg7, we used
455 AlphaFold-2.0 Multimer[75] to model the structure of these proteins alone or in complex with
456 each other. Atg7, which functions as a homodimer, has two globular domains: An N-
457 terminal domain and a C-terminal domain that are separated by a short flexible linker.
458 The C-terminal domain is further divided into the adenylation and extreme C-terminal
459 domains (Figure 7A-B)[76]. Ezrin comprises an N-terminal FERM (four-point one, Ezrin,
460 Radixin, Moesin) domain (subdivided into three subdomains- F1, F2, and F3), α-helical
461 domain, and a C-terminal ERM Association domain (C-ERMAD) (Figure 7C)[67]. When
462 unphosphorylated, Ezrin remains in a closed state where N and C terminal domains
463 interact, and the central alpha-helical hinge region bends to form a “clamshell-like”
464 structure. Upon phosphorylation of T567 and binding to PIP2, Ezrin acquires an open
465 conformation[77]. We also modeled both conformations of Ezrin using Alpha-fold (Figure
466 7D; see Methods for details of modeling).

467 We additionally utilized Alpha-fold 2.0 multimer to predict the structure of the
468 complex formed between the closed conformation of Ezrin and the homodimer of Atg7

469 (Figure 7E). Alpha-fold 2.0 multimer, in conjunction with CABS-Flex 2.0 and PyMol, were
470 used to predict and assess conformational changes in Atg7 and Ezrin after binding each
471 other (Figure 7F). When Ezrin binds Atg7, it is predicted to undergo drastic conformational
472 changes in its α-helical domain, which is pulled towards the ERMAD and FERM domains,
473 whereas the changes in the Atg7 dimer structure after Ezrin binding are minimal (Figure
474 7F). These modeling analyses strongly suggested a direct interaction between Ezrin and
475 Atg7, which we set out to test empirically next.

476 To probe for an interaction between Ezrin and Atg7, we performed co-
477 immunoprecipitation (Co-IP) in HEK293T cells overexpressing Myc-tagged Atg7 (Atg7-
478 Myc) and HA-tagged WT Ezrin. To understand how the open or closed conformation of
479 Ezrin would impact the Atg7 interaction, we also conducted Co-IPs with modulation of
480 Ezrin phosphorylation levels: phospho-mimetic T567D ("TD", open) and phospho-dead
481 T567A ("TA", closed) Ezrin. We found that WT Ezrin or phospho-dead Ezrin
482 coimmunoprecipitated with Myc-Atg7, indicating that Atg7 interacts with WT Ezrin or
483 phospho-dead Ezrin (Figure 7G). However, the interaction between Atg7 and phospho-
484 mimetic Ezrin was significantly reduced (Figure 7H). Together with the structural modeling,
485 these results suggest that Atg7 interacts directly with Ezrin in a
486 phosphorylation/conformation-dependent manner. These findings align well with our
487 Ezrin BioID data (Figure 6), in which Atg7 lost interaction with Ezrin in LRRK2 G2019S$^{ki/ki}$
488 astrocytes. These findings also indicate that Atg7 may play a role in regulating astrocyte
489 morphogenesis, and this function of Atg7 may be altered in LRRK2 G2019S$^{ki/ki}$ astrocytes.

490 Due to the impaired interaction between Atg7 and Ezrin when Ezrin is in its
491 phospho-mimetic (open) state, we hypothesized that altered Atg7 function contributes to
492 impaired astrocyte morphology in LRRK2 G2019S$^{ki/ki}$ mice. To test this hypothesis, we
493 developed a short hairpin RNA (shRNA) that targets both rat and mouse *Atg7,* which
494 effectively reduced *Atg7* mRNA in mouse cells (Figure S10A). Knockdown of Atg7 in rat
495 astrocytes significantly reduced neuron-induced astrocyte morphogenesis *in vitro* in a
496 neuron-astrocyte co-culture assay (Figure S10B-C).

497 To elucidate the necessity of Atg7 in regulating astrocyte morphology *in vivo*, we
498 introduced shControl or shAtg7 into a sparse population of cortical astrocytes in WT and
499 LRRK2 G2019S$^{ki/ki}$ mice by using PALE. We found that Atg7 knockdown in WT astrocytes
500 led to a significant reduction in astrocyte territory volume and morphological complexity,
501 resembling the LRRK2 G2019S$^{ki/ki}$ astrocytes transfected with shControl (Figure 7I-K).
502 Atg7 knockdown in LRRK2 G2019S$^{ki/ki}$ astrocytes did not further reduce their territory
503 volume (Figure 7J) but significantly improved their morphological complexity (Figure 7K).
504 Overall, these data reveal an essential role for Atg7 in astrocyte morphological complexity
505 and suggest that disruptions in Atg7 function in astrocytes contribute to the altered
506 astrocyte morphology observed in LRRK2 G2019S$^{ki/ki}$ mice.

507 DISCUSSION

508 Here, we describe a previously unknown role for Lrrk2, a PD-linked gene, in
509 controlling astrocyte morphological complexity by regulating the phosphorylation state of
510 ERM proteins. In the presence of LRRK2 G2019S mutation, we found enhanced ERM
511 phosphorylation in human and mouse cortical astrocytes. ERM hyperphosphorylation in
512 the LRRK2 G2019S background is specific to a subset of the ACC and MOp astrocytes

513 of juvenile and adult mice. The hyperphosphorylation of ERM proteins in these regions
514 occurred concurrently with dysregulated astrocytic morphology and synapse numbers
515 and activity. These observations prompted us to test how shifting the balance of the ERM
516 phosphorylation status in astrocytes impacts astrocyte morphology and synaptic
517 connectivity. We found that overexpression of a phospho-dead Ezrin, specifically in
518 astrocytes, is sufficient to rescue both the morphological deficits of astrocytes themselves
519 as well as the number and function of excitatory synapses within the ACC of the LRRK2
520 G2019S$^{ki/ki}$ mice. However, the same manipulation is detrimental in WT astrocytes. Taken
521 together, these results support a model that Lrrk2 activity in astrocytes regulates a tight
522 balance between phosphorylated and unphosphorylated ERM proteins in astrocytes, and
523 pushing this balance in either direction impairs astrocytes' morphology and synaptic
524 functions.

525 **How does ERM phosphorylation control astrocyte morphology and**
526 **synaptogenic functions?**

527 The canonical function of ERM proteins is linking the actin cytoskeleton with the
528 plasma membrane, thus allowing cellular process outgrowth and morphogenesis[64]. Our
529 findings suggest that disruptions in the interaction between Ezrin and a core autophagy-
530 related protein, Atg7, contribute to the altered astrocyte morphology observed in LRRK2
531 G2019S$^{ki/ki}$ mice. *In vivo* Ezrin interactome in astrocytes included several other proteins
532 related to autophagy, which changed their proximity to Ezrin in the LRRK2 G2019S$^{ki/ki}$
533 astrocytes, compared to WT astrocytes. These observations indicate that dysregulated
534 autophagy due to ERM hyperphosphorylation may underlie the deficits we observed in
535 astrocytes.

536 Another intriguing observation is that, *in vivo*, knocking down Atg7 in WT
537 astrocytes reduces astrocyte morphological complexity. Atg7 is a homodimeric E1-like
538 enzyme that is essential for autophagy, a process crucial for maintaining cellular
539 homeostasis by degrading and recycling damaged organelles and proteins[73]. The
540 presence of autophagic dysregulation in the context of neurodegenerative diseases,
541 including PD-associated LRRK2 mutations, is well-documented[31,78,72]. However, whether
542 autophagy plays a role in astrocyte morphology and its synaptogenic functions is not
543 known. Moreover, how LRRK2 G2019S mutation impacts autophagy in astrocytes is not
544 yet elucidated. It is tempting to speculate that the depletion of Atg7 disrupts autophagic
545 flux, accumulating damaged organelles and proteins within astrocytes, potentially
546 compromising their structural integrity and function.

547 However, even without Atg7, other forms of autophagy can still occur[79,80],
548 suggesting that the role of Atg7 in astrocyte morphogenesis may be independent of its
549 canonical role in autophagy. For example, Atg7 is implicated in various endocytic
550 pathways, including LC3-associated endocytosis and phagocytosis, processes crucial for
551 cellular clearance and process remodeling[81,82]. Our findings also pinpoint a role for Ezrin
552 (and other ERM proteins) in autophagy regulation. In agreement, there is emerging
553 evidence linking Ezrin to molecular pathways regulating autophagy[83]. Through molecular
554 modeling and biochemical methods, we found evidence for a direct interaction between
555 Atg7 and unphosphorylated Ezrin. Future studies would be highly fruitful if we could
556 determine how this interaction impacts astrocyte cell biology.

557 Astrocytes control synapse formation and function through cell adhesion
558 molecules and secreted proteins that signal to neurons[14]. It is plausible that ERM

559 phosphorylation regulates synaptogenic protein secretion from astrocytes via autophagy-
560 related pathways. Another alternative explanation is the role of astrocytic phospho-ERM
561 proteins in controlling synapse elimination via phagocytosis by astrocytes. In agreement
562 with this possibility, a recent study found that synapses are more likely to be eliminated if
563 phospho-ERM proteins were localized to peri-synaptic astrocyte processes in ALS patient
564 brains and mouse models[84]. Future research investigating the complex relationships
565 between Lrrk2, ERM, and autophagy in astrocytes will be necessary to test these
566 intriguing possibilities.

567 **Implications for Therapeutic Development**

568 LRRK2 G2019S$^{ki/ki}$ mice do not recapitulate motor symptoms of PD because there
569 is no detectable dopaminergic neuron loss in these mice[30,43]. However, these mice serve
570 as good models for the non-motor (prodromal) PD symptoms seen in LRRK2 G2019S
571 carriers[3]. These non-motor symptoms, which arise long before motor dysfunction in PD,
572 indicate aberrant synaptic connectivity within multiple brain circuits, including the cortex,
573 long before the death of dopaminergic neurons[85].

574 In agreement, LRRK2 G2019S$^{ki/ki}$ mice display early circuit dysfunction and non-
575 motor symptoms akin to prodromal PD. Previous studies showed that LRRK2 G2019S$^{ki/ki}$
576 mice have deficits in attention and goal-directed learning and differential response to
577 stress[33,35,86]. Our findings showing synaptic deficits in the ACC of LRRK2 G2019S$^{ki/ki}$ mice
578 (Figure 2-3) fit well with these studies because the ACC is a brain region that controls
579 attention, goal-directed actions, and mood[87,88]. Furthermore, we observed synaptic
580 deficits in the ACC of LRRK2 G2019S$^{ki/ki}$ mice concurrently with astrocyte morphological
581 deficits located in the ACC and MOp.

582 Why do ERM phosphorylation and synaptic deficits happen in specific brain
583 regions of LRRK2 G2019S$^{ki/ki}$ mice? Adult cortical astrocytes are heterogeneous in their
584 gene expression, morphology, and function[89,90]. Interestingly, cortical astrocyte
585 heterogeneity is controlled by layer-specific neuron heterogeneity[89,90]. It is plausible that
586 neurons and astrocytes in different cortical regions have varying levels of LRRK2 and
587 diverse susceptibilities to LRRK2 mutations. The ACC and MOp may heavily depend on
588 LRRK2 to maintain synaptic integrity and astrocyte function. Future studies investigating
589 the impacts of LRRK2 G2019S in cortical neurons and astrocytes' transcriptional profiles
590 may help explain why region-specific impact of this mutation in astrocytes.

591 In sum, our findings reveal a critical function for Lrrk2 in astrocyte development
592 and synaptic connectivity, suggesting that Lrrk2-mediated ERM hyperphosphorylation in
593 astrocytes is an early mediator of PD pathogenesis. This astrocytic dysfunction could
594 directly contribute to synaptic deficits observed in the prodromal stages of PD. Moreover,
595 our data indicate that restoring astrocyte function, even post-development could be a
596 promising strategy for treating excitatory synaptic pathology. Identifying the molecular
597 mechanisms by which Lrrk2 controls ERM phosphorylation and the specific phosphatases
598 involved could lead to new therapeutic targets for PD. Future studies aimed to elucidate
599 the molecular mechanisms through which Lrrk2 controls ERM phosphorylation and to
600 identify the phosphatases required to that maintain the tight balance of ERM
601 phosphorylation in astrocytes are likely to reveal new targets for PD therapeutics.

602 **FIGURE LEGENDS**

603 **Figure 1: ERM phosphorylation is impaired in PD patients carrying LRRK2 G2019S**
604 **mutation.** (A) Schematic representation of analyzed human brain regions for phospho-

605 ERM staining, frontal cortex. (B) Representative confocal images of GFAP (green) and
606 ERM phosphorylation (purple) in the frontal cortex of human control subjects or human
607 PD patients carrying LRRK2 G2019S mutation carriers at age >80 years old. Scale bar,
608 200 μm. (C) Quantification of GFAP integrated density in (B), n = 4 (Human control, 3
609 males and 1 female), 3 (LRRK2 G2019S mutation carriers, 2 males and 1 female)
610 subjects, nested t-test, unpaired Two-tailed t-test. t (18) = 3.612, p = 0.0020.
611 Quantification of phospho-ERM integrated density in (B), n = 4 (Human control, 3 males
612 and 1 female), 3 (LRRK2 G2019S mutation carriers, 2 males and 1 female) subjects,
613 nested t-test, unpaired Two-tailed t-test. t (4) = 3.551, p = 0.0238. Grey dots are the data
614 acquired from each image. Black dots are the averaged data acquired from each control
615 subject. Blue dots are the averaged data acquired from each LRRK2 G2019S mutation
616 carrier. (D) Schematic representation of analyzed mouse brain regions for phospho-ERM
617 staining, the anterior cingulate cortex (ACC), and the primary motor cortex (MOp). (E-F)
618 Representative confocal images of phospho-ERM (purple) in the ACC and the MOp of
619 WT or LRRK2 G2019S$^{ki/ki}$ Aldh1L1-eGFP mice at P21. Scale bar, 10 μm. (G-H)
620 Representative confocal images of phospho-ERM (purple) in the ACC and MOp of WT or
621 LRRK2 G2019S$^{ki/ki}$ Aldh1L1-eGFP mice at P21. Scale bar, 200 μm. (I) Quantification of
622 phospho-ERM integrated density in (G-H), n = 4 (WT, 2 males and 2 females), 4 (LRRK2
623 G2019S$^{ki/ki}$, 2 males and 2 females) mice, For phospho-ERM quantification in the ACC,
624 nested t-test, unpaired two-tailed t-test. t (6) = 3.295, p = 0.0165. For phospho-ERM
625 quantification in the MOp, nested t-test, unpaired two-tailed t-test. t (24) = 3.462, p = 0.002.
626 (J-K) Representative confocal images of phospho-ERM (purple) in the ACC and MOp of
627 WT or LRRK2 G2019S$^{ki/ki}$ Aldh1L1-eGFP mice at P84. Scale bar, 200 μm. n = 4 (WT, 2

628 males and 2 females), 4 (LRRK2 G2019S$^{ki/ki}$, 2 males and 2 females) mice. (L)
629 Quantification of phospho-ERM integrated density in (J-K), n = 4 (WT, 2 males and 2
630 females), 4 (LRRK2 G2019S$^{ki/ki}$, 2 males and 2 females) mice, For phospho-ERM
631 quantification in the ACC, nested t-test, unpaired Two-tailed t-test. t (46) = 6.173, p <
632 0.0001. For phospho-ERM quantification in the MOp, nested t-test, unpaired Two-tailed
633 t-test. t (10) = 3.146, p = 0.0104. Grey dots are the data acquired from each image. Black
634 dots are the averaged data acquired from each WT mouse. Blue dots are the averaged
635 data acquired from each LRRK2 G2019S$^{ki/ki}$ mouse.

636 **Figure 2: LRRK2 G2019S affects excitatory and inhibitory synapse numbers in the**
637 **ACC and MOp.** (A) Schematic representation of analyzed brain regions (ACC and MOp)
638 for excitatory and inhibitory synapse numbers. (B) Schematic representations of
639 methodologies used to quantify the VGluT1-PSD95 and VGAT-GEPHYRIN colocalized
640 puncta. (C) Representative images from the ventral ACC of WT and LRRK2 G2019S$^{ki/ki}$
641 mice that were stained with VGluT1 and PSD95 antibodies at P84. Scale bar, 10 μm. (D)
642 Quantification of VGluT1-PSD95 co-localized puncta, normalized using the means of WT
643 values in the ventral ACC L1 and L2-3. n = 5 (WT, 3 males and 2 females), 5 (LRRK2
644 G2019S$^{ki/ki}$, 3 males and 2 females) mice. Nested One-way ANOVA [F (3, 56) = 12.48, p
645 < 0.0001], Bonferroni's multiple comparisons test revealed a significant difference
646 between WT ACC L1 and LRRK2 G2019S$^{ki/ki}$ ACC L1 (p < 0.0001, 95% C.I. = [16.83,
647 52.83]), and between WT ACC L2-3 and LRRK2 G2019S$^{ki/ki}$ ACC L2-3 (p = 0.0002, 95%
648 C.I. = [14.73, 50.74]). alpha = 0.05. (E) Representative images from the MOp of WT and
649 LRRK2 G2019S$^{ki/ki}$ mice that were stained with VGluT1 and PSD95 antibodies at P84.
650 Scale bar, 10 μm. (F) Quantification of VGluT1-PSD95 co-localized puncta, normalized

651 using the means of WT values in the MOp L1 and L2-3. n = 5 (WT, 3 males and 2 females),
652 5 (LRRK2 G2019S$^{ki/ki}$, 3 males and 2 females) mice. Nested One-way ANOVA [F (3, 56)
653 = 0.3681, p = 0.7763], Bonferroni's multiple comparisons test revealed a significant
654 difference between WT MOp L1 and LRRK2 G2019S$^{ki/ki}$ MOp L1 (p = 0.7358, 95% C.I. =
655 [-18.62, 42.83]), and between WT MOp L2-3 and LRRK2 G2019S$^{ki/ki}$ MOp L2-3 (p >
656 0.9999, 95% C.I. = [-27.51, 33.94]). alpha = 0.05. (G) Representative images from the
657 ventral ACC of WT and LRRK2 G2019S$^{ki/ki}$ mice that were stained with VGAT and
658 GEPHYRIN antibodies at P84. Scale bar, 10 μm. (H) Quantification of VGAT-GEPHYRIN
659 co-localized puncta, normalized using the means of WT values in the ventral ACC L1 and
660 L2-3. n = 4 (WT, 2 males and 2 females), 4 (LRRK2 G2019S$^{ki/ki}$, 2 males and 2 females)
661 mice. Nested One-way ANOVA [F (3, 43) = 0.1155, p = 0.9505], Bonferroni's multiple
662 comparisons test revealed a significant difference between WT ACC L1 and LRRK2
663 G2019S$^{ki/ki}$ ACC L1 (p > 0.9999, 95% C.I. = [-28.54, 20.66]), and between WT ACC L2-3
664 and LRRK2 G2019S$^{ki/ki}$ ACC L2-3 (p > 0.9999, 95% C.I. = [-20.71, 29.60]). alpha = 0.05.
665 (I) Representative images from MOp of WT and LRRK2 G2019S$^{ki/ki}$ mice that were stained
666 with VGAT and GEPHYRIN antibodies at P84. Scale bar, 10 μm. (J) Quantification of
667 VGAT-GEPHYRIN co-localized puncta, normalized using the means of WT values in
668 MOp L1 and L2-3. n = 6 (WT, 3 males and 3 females), 6 (LRRK2 G2019S$^{ki/ki}$, 3 males
669 and 3 females) mice. Nested One-way ANOVA [F (3, 68) = 25.88, p < 0.0001],
670 Bonferroni's multiple comparisons test revealed a significant difference between WT MOp
671 L1 and LRRK2 G2019S$^{ki/ki}$ MOp L1 (p < 0.0001, 95% C.I. = [-60.89, -30.43]), and between
672 WT MOp L2-3 and LRRK2 G2019S$^{ki/ki}$ MOp L2-3 (p < 0.0001, 95% C.I. = [-51.48, -21.02]).
673 alpha = 0.05. Grey dots are the data acquired from each synapse image. Black dots are

674 the averaged data acquired from each WT mouse. Blue dots are the averaged data
675 acquired from each LRRK2 G2019S$^{ki/ki}$ mouse.

676 **Figure 3: LRRK2 G2019S affects excitatory and inhibitory synapse function in the**
677 **ACC and MOp.** (A) Representative mEPSC traces from the ventral ACC L2-3 pyramidal
678 neurons in acute brain slices of WT and LRRK2 G2019S$^{ki/ki}$ mice. (B) Cumulative
679 probability plots and quantification of synaptic event frequency, n = 15 (WT), 13 (LRRK2
680 G2019S$^{ki/ki}$) neurons from 4 mice per genotype. Kolmogorov-Smirnov test (D = 0.504, p
681 < 0.001). The average frequency of mEPSC in WT (2.521 ± 0.3846) and LRRK2
682 G2019S$^{ki/ki}$ (0.8691 ± 0.1309) mice. Unpaired Two-tailed t-test [t (26) = 3.828, p = 0.0007].
683 (C) Cumulative probability plots and quantification of synaptic event amplitude, n = 14
684 (WT), 12 (LRRK2 G2019S$^{ki/ki}$) neurons from 4 mice per genotype. Kolmogorov-Smirnov
685 test (D = 0.194, p < 0.0001). The average amplitude of mEPSC in WT (7.826 ± 0.8259)
686 and LRRK2 G2019S$^{ki/ki}$ (6.959 ± 0.9015) mice. Unpaired t-test [t (24) = 0.7093, p = 0.485].
687 (D) Representative mIPSC traces from MOp L2-3 pyramidal neurons in acute brain slices
688 of WT and LRRK2 G2019S$^{ki/ki}$ mice. (E) Cumulative probability plots and quantification of
689 synaptic event frequency, n = 12 (WT), 11 (LRRK2 G2019S$^{ki/ki}$) neurons from 4 mice per
690 genotype. Kolmogorov-Smirnov test (D = 0.424, p < 0.0001). The average frequency of
691 mIPSC in WT (0.7606 ± 0.06816) and LRRK2 G2019S$^{ki/ki}$ (1.312 ± 0.1041) mice.
692 Unpaired Two-tailed t-test [t (21) = 4.503, p = 0.0002]. (F) Cumulative probability plots
693 and quantification of synaptic event amplitude, n = 12 (WT), 11 (LRRK2 G2019S$^{ki/ki}$)
694 neurons from 4 mice per genotype. Kolmogorov-Smirnov test (D = 0.382, p < 0.0001).
695 The average amplitude of mIPSC in WT (8.776 ± 0.4961) and LRRK2 G2019S$^{ki/ki}$ (9.921

696 ± 0.5043) mice. Unpaired t-test [t (21) = 1.617, p = 0.1209]. Data are presented as mean
697 ± s.e.m.

698 **Figure 4: Overexpression of phospho-dead Ezrin in adult LRRK2 G2019S$^{ki/ki}$**
699 **astrocytes restores excitatory synapse number and function in the ventral ACC.** (A)
700 Representative images from the ventral ACC of WT and LRRK2 G2019S$^{ki/ki}$ mice injected
701 with AAV-HA-tagged-WT Ezrin or AAV-HA-tagged-Phospho-dead Ezrin that were stained
702 with HA and phospho-ERM antibodies at P84. Scale bar, 200 µm. n = 6 (WT + WT Ezrin
703 O/E, 3 males and 3 females), 5 (WT + Phospho-dead Ezrin O/E, 3 males and 2 females),
704 6 (LRRK2 G2019S$^{ki/ki}$ + WT Ezrin O/E, 3 males and 3 females), 6 (LRRK2 G2019S$^{ki/ki}$ +
705 Phospho-dead Ezrin O/E, 3 males and 3 females) mice. (B) Quantification of phospho-
706 ERM integrated density in (A). n = 6 (WT + WT Ezrin O/E, 3 males and 3 females), 6 (WT
707 + Phospho-dead Ezrin O/E, 3 males and 3 females), 6 (LRRK2 G2019S$^{ki/ki}$ + WT Ezrin
708 O/E, 3 males and 3 females), 6 (LRRK2 G2019S$^{ki/ki}$ + Phospho-dead Ezrin O/E, 3 males
709 and 3 females) mice. One-way ANOVA [F (3, 20) = 31.62, p < 0.0001], Bonferroni's
710 multiple comparisons test revealed a significant difference between WT + WT Ezrin O/E
711 and LRRK2 G2019S$^{ki/ki}$ + WT Ezrin O/E (p < 0.0001, 95% C.I. = [-34272667, -17645403]),
712 and between LRRK2 G2019S$^{ki/ki}$ + WT Ezrin O/E and LRRK2 G2019S$^{ki/ki}$ + Phospho-
713 dead Ezrin O/E (p < 0.0001, 95% C.I. = [11069274, 27696537]). There were no
714 differences between WT + WT Ezrin O/E and WT + Phospho-dead Ezrin O/E (p = 0.3065,
715 95% C.I. = [-14207483, 2419780]), and between WT + Phospho-dead Ezrin O/E and
716 LRRK2 G2019S$^{ki/ki}$ + Phospho-dead Ezrin O/E (p > 0.9999, 95% C.I. = [-8995910,
717 7631353]), alpha = 0.05. (C) Representative images from the ventral ACC L1 of WT and
718 LRRK2 G2019S$^{ki/ki}$ mice injected with AAV-HA-tagged-WT Ezrin or AAV-HA-tagged-

719 Phospho-dead Ezrin that were stained with VGluT1 and PSD95 antibodies at P84. Scale
720 bar, 10 μm. Quantification of VGluT1-PSD95 co-localized puncta, normalized using the
721 means of WT mice injected with AAV-HA-tagged-WT Ezrin in the ventral ACC L1. n = 6
722 (WT + WT Ezrin O/E, 3 males and 3 females), 5 (WT + Phospho-dead Ezrin O/E, 3 males
723 and 2 females), 6 (LRRK2 G2019S$^{ki/ki}$ + WT Ezrin O/E, 3 males and 3 females), 6 (LRRK2
724 G2019S$^{ki/ki}$ + Phospho-dead Ezrin O/E, 3 males and 3 females) mice. One-way ANOVA
725 [F (3, 19) = 5.882, p = 0.0051], Bonferroni's multiple comparisons test revealed a
726 significant difference between WT + WT Ezrin O/E and WT + Phospho-dead Ezrin O/E (p
727 = 0.0493, 95% C.I. = [0.05586, 53.21]), between WT + WT Ezrin O/E and LRRK2
728 G2019S$^{ki/ki}$ + WT Ezrin O/E (p = 0.0269, 95% C.I. = [2.396, 53.08]), and between LRRK2
729 G2019S$^{ki/ki}$ + WT Ezrin O/E and LRRK2 G2019S$^{ki/ki}$ + Phospho-dead Ezrin O/E (p = 0.049,
730 95% C.I. = [-50.77, -0.08163]). There were no differences between WT + WT Ezrin O/E
731 and LRRK2 G2019S$^{ki/ki}$ + Phospho-dead Ezrin O/E (p > 0.9999, 95% C.I. = [-23.03,
732 27.66]), between WT + Phospho-dead Ezrin O/E and LRRK2 G2019S$^{ki/ki}$ + WT Ezrin O/E
733 (p > 0.9999, 95% C.I. = [-25.48, 27.68]), and between WT + Phospho-dead Ezrin O/E and
734 LRRK2 G2019S$^{ki/ki}$ + Phospho-dead Ezrin O/E (p = 0.0863, 95% C.I. = [-50.90, 2.259]),
735 alpha = 0.05. (D) Representative images from the ventral ACC L2-3 of WT and LRRK2
736 G2019S$^{ki/ki}$ mice injected with AAV-HA-tagged-WT Ezrin or AAV-HA-tagged-Phospho-
737 dead Ezrin that were stained with VGluT1 and PSD95 antibodies at P84. Scale bar, 10
738 μm. Quantification of VGluT1-PSD95 co-localized puncta, normalized using the means of
739 WT mice injected with AAV-HA-tagged-WT Ezrin in the ventral ACC L2-3. n = 6 (WT +
740 WT Ezrin O/E, 3 males and 3 females), 5 (WT + Phospho-dead Ezrin O/E, 3 males and
741 2 females), 6 (LRRK2 G2019S$^{ki/ki}$ + WT Ezrin O/E, 3 males and 3 females), 6 (LRRK2

742 G2019S$^{ki/ki}$ + Phospho-dead Ezrin O/E, 3 males and 3 females) mice. One-way ANOVA
743 [F (3, 18) = 10.45, p = 0.0003], Bonferroni's multiple comparisons test revealed a
744 significant difference between WT + WT Ezrin O/E and WT + Phospho-dead Ezrin O/E (p
745 = 0.0041, 95% C.I. = [8.857, 55.39]), between WT + WT Ezrin O/E and LRRK2 G2019S$^{ki/ki}$
746 + WT Ezrin O/E (p = 0.0016, 95% C.I. = [11.67, 56.22]), between WT + Phospho-dead
747 Ezrin O/E and LRRK2 G2019S$^{ki/ki}$ + Phospho-dead Ezrin O/E (p = 0.0232, 95% C.I. = [-
748 47.19.67, -2.636]) and between LRRK2 G2019S$^{ki/ki}$ + WT Ezrin O/E and LRRK2
749 G2019S$^{ki/ki}$ + Phospho-dead Ezrin O/E (p = 0.0092, 95% C.I. = [-47.97.77, -5.494]). There
750 were no differences between WT + WT Ezrin O/E and LRRK2 G2019S$^{ki/ki}$ + Phospho-
751 dead Ezrin O/E (p > 0.9999, 95% C.I. = [-15.06, 29.49]), and between WT + Phospho-
752 dead Ezrin O/E and LRRK2 G2019S$^{ki/ki}$ + WT Ezrin O/E (p > 0.9999, 95% C.I. = [-20.45,
753 24.10]), alpha = 0.05. (E) Representative mEPSC traces from the ventral ACC L2-3
754 pyramidal neurons in acute brain slices of WT and LRRK2 G2019S$^{ki/ki}$ mice injected with
755 AAV-HA-tagged-WT Ezrin or AAV-HA-tagged-Phospho-dead Ezrin. (F) Cumulative
756 probability plots and quantification of synaptic event frequency. n = 14 (WT + WT Ezrin
757 O/E), 15 (WT + Phospho-dead Ezrin O/E), 11 (LRRK2 G2019S$^{ki/ki}$ + WT Ezrin O/E), 14
758 (LRRK2 G2019S$^{ki/ki}$ + Phospho-dead Ezrin O/E) neurons from 4 mice per condition.
759 Kruskal-Wallis test [H (3) = 36.83, p < 0.0001]. Average frequency of mEPSC in WT +
760 WT Ezrin O/E (1.555 ± 0.1125), WT + Phospho-dead Ezrin O/E (0.8416 ± 0.05145),
761 LRRK2 G2019S$^{ki/ki}$ + WT Ezrin O/E (0.7154 ± 0.05959), and LRRK2 G2019S$^{ki/ki}$ +
762 Phospho-dead Ezrin O/E (1.253 ± 0.04424) mice. The posthoc Dunn's test with
763 Bonferroni adjustments showed to be significant for WT + WT Ezrin O/E vs. WT +
764 Phospho-dead Ezrin O/E (p < 0.0001), WT + WT Ezrin O/E vs. LRRK2 G2019S$^{ki/ki}$ + WT

765 Ezrin O/E ($p < 0.0001$), WT + Phospho-dead Ezrin O/E vs. LRRK2 G2019S$^{ki/ki}$ + Phospho-
766 dead Ezrin O/E ($p = 0.0084$), and LRRK2 G2019S$^{ki/ki}$ + WT Ezrin O/E vs. LRRK2
767 G2019S$^{ki/ki}$ + Phospho-dead Ezrin O/E ($p = 0.0005$). The posthoc Dunn's test with
768 Bonferroni adjustments revealed no significant difference between WT + WT Ezrin O/E
769 and LRRK2 G2019S$^{ki/ki}$ + Phospho-dead Ezrin O/E ($p > 0.9999$) and between WT +
770 Phospho-dead Ezrin O/E and LRRK2 G2019S$^{ki/ki}$ + WT Ezrin O/E ($p > 0.9999$). (G)
771 Cumulative probability plots and quantification of synaptic event amplitude. n = 11 (WT +
772 WT Ezrin O/E), 15 (WT + Phospho-dead Ezrin O/E), 11 (LRRK2 G2019S$^{ki/ki}$ + WT Ezrin
773 O/E), 13 (LRRK2 G2019S$^{ki/ki}$ + Phospho-dead Ezrin O/E) neurons from 4 mice per
774 condition. Kruskal-Wallis test [H (3) = 7.051, $p = 0.0703$]. Average amplitude of mEPSC
775 in WT + WT Ezrin O/E (4.873 ± 0.1034), WT + Phospho-dead Ezrin O/E (6.339 ± 0.4284),
776 LRRK2 G2019S$^{ki/ki}$ + WT Ezrin O/E (5.354 ± 0.2988), and LRRK2 G2019S$^{ki/ki}$ + Phospho-
777 dead Ezrin O/E (5.591 ± 0.2247) mice. The posthoc Dunn's test with Bonferroni
778 adjustments revealed no significant difference for WT + WT Ezrin O/E vs. WT + Phospho-
779 dead Ezrin O/E ($p = 0.0688$), WT + WT Ezrin O/E vs. LRRK2 G2019S$^{ki/ki}$ + WT Ezrin O/E
780 ($p > 0.9999$), WT + Phospho-dead Ezrin O/E vs. LRRK2 G2019S$^{ki/ki}$ + Phospho-dead
781 Ezrin O/E ($p > 0.9999$), and LRRK2 G2019S$^{ki/ki}$ + WT Ezrin O/E vs. LRRK2 G2019S$^{ki/ki}$ +
782 Phospho-dead Ezrin O/E ($p > 0.9999$), WT + WT Ezrin O/E vs. LRRK2 G2019S$^{ki/ki}$ +
783 Phospho-dead Ezrin O/E ($p = 0.3605$), and WT + Phospho-dead Ezrin O/E vs. LRRK2
784 G2019S$^{ki/ki}$ + WT Ezrin O/E ($p = 0.9468$). alpha = 0.05. Data are presented as mean ±
785 s.e.m.

786 **Figure 5: Astrocytic LRRK2 controls astrocyte morphology by balancing ERM**
787 **phosphorylation levels *in vivo*.** (A) Images of ACC and MOp L2-3 WT and LRRK2

788 G2019S$^{ki/ki}$ astrocytes at P21 expressing PB-mCherry-CAAX ± Phospho-dead Ezrin.
789 Astrocyte territory in cyan. Scale bar, 10 µm. (B) Average territory volumes of P21
790 astrocytes. n = 16 (WT; 6 mice), 18 (WT + Phospho-dead Ezrin O/E; 6 mice), 16 (LRRK2
791 G2019S$^{ki/ki}$; 6 mice), 17 (LRRK2 G2019S$^{ki/ki}$ + Phospho-dead Ezrin O/E; 6 mice).
792 Statistical significance was determined by One-way ANOVA [F (3, 20) = 7.987, p =
793 0.0011], Bonferroni multiple comparisons revealed a significant difference between WT
794 and LRRK2 G2019S$^{ki/ki}$ (p = 0.0178, 95% C.I. = [0.4542, 6.313]), between WT and WT +
795 Phospho-dead Ezrin O/E (p = 0.0037, 95% C.I. = [1.132, 6.991]), and between WT +
796 Phospho-dead Ezrin O/E and LRRK2 G2019S$^{ki/ki}$ + Phospho-mimetic Ezrin O/E (p =
797 0.0165, 95% C.I. = [-6.346, -0.4875]), and no differences between WT and LRRK2
798 G2019S$^{ki/ki}$ + Phospho-mimetic Ezrin O/E (p > 0.9999, 95% C.I. = [-2.284, 3.574]),
799 between LRRK2 G2019S$^{ki/ki}$ and WT + Phospho-dead Ezrin O/E (p > 0.9999, 95% C.I. =
800 [-2.251, 3.608]), and between LRRK2 G2019S$^{ki/ki}$ and LRRK2 G2019S$^{ki/ki}$ + Phospho-
801 mimetic Ezrin O/E (p = 0.0763, 95% C.I. = [-5.668, 0.1908]), alpha = 0.05. Data points
802 are mouse averages. (C) Quantification of astrocyte branching complexity. n = 16 (WT; 6
803 mice), 18 (WT + Phospho-dead Ezrin O/E; 6 mice), 16 (LRRK2 G2019S$^{ki/ki}$; 6 mice), 17
804 (LRRK2 G2019S$^{ki/ki}$ + Phospho-dead Ezrin O/E; 6 mice). Two-way ANOVA for repeated
805 measures. Main effects of conditions [F (2.505, 3305) = 158.4, p < 0.0001] and radius [F
806 (88, 1602) = 218.5, p < 0.0001] and interaction [F (264, 3958) = 10.62, p < 0.0001].
807 Bonferroni multiple comparisons revealed a significant difference between WT and
808 LRRK2 G2019S$^{ki/ki}$ (p < 0.0001, 95% C.I. = [16.09, 26.40]), between WT and WT +
809 Phospho-dead Ezrin O/E (p < 0.0001, 95% C.I. = [29.06, 39.54]), between LRRK2
810 G2019S$^{ki/ki}$ and WT + Phospho-dead Ezrin O/E (p < 0.0001, 95% C.I. = [7.6, 18.52]),

811 between LRRK2 G2019S$^{ki/ki}$ and LRRK2 G2019S$^{ki/ki}$ + Phospho-dead Ezrin O/E (p <
812 0.0001, 95% C.I. = [-22.19, -13.43]), and between WT + Phospho-dead Ezrin O/E and
813 LRRK2 G2019S$^{ki/ki}$ + Phospho-dead Ezrin O/E (p < 0.0001, 95% C.I. = [-37.02, -24.72]),
814 and no difference between WT and LRRK2 G2019S$^{ki/ki}$ + Phospho-dead Ezrin O/E (p =
815 0.5469, 95% C.I. = [-1.932, 8.796]). (D) A proposed working model of how Ezrin in
816 astrocytes transitions between open and closed conformation and Lrrk2 regulates
817 astrocyte morphogenesis by modulating this transition. (E) Images of ACC and MOp L2-
818 3 astrocytes at P21 expressing shControl-mCherry-CAAX or sh*Lrrk2*-mCherry-CAAX ±
819 Phospho-mimetic Ezrin. Astrocyte territory in cyan. Scale bar, 10 µm. (F) Average territory
820 volumes of P21 astrocytes. n = 18 (shControl; 6 mice), 18 (shControl + Phospho-mimetic
821 Ezrin O/E; 5 mice), 22 (sh*Lrrk2*; 6 mice), 19 (sh*Lrrk2* + Phospho-mimetic Ezrin O/E; 6
822 mice). Statistical significance was determined by One-way ANOVA [F (3, 19) = 5.47, p =
823 0.0070], Bonferroni multiple comparisons revealed a significant difference between
824 shControl and sh*Lrrk2* (p = 0.0132, 95% C.I. = [0.4928, 5.387]), and between sh*Lrrk2* and
825 sh*Lrrk2* + Phospho-mimetic Ezrin O/E (p = 0.0152, 95% C.I. = [-5.337, -0.4428]), and no
826 differences between shControl and shControl + Phospho-mimetic Ezrin O/E (p > 0.9999,
827 95% C.I. = [-1.495, 3.639]), between shControl and sh*Lrrk2* + Phospho-mimetic Ezrin O/E
828 (p > 0.9999, 95% C.I. = [-2.397, 2.497]), and between shControl + Phospho-mimetic Ezrin
829 O/E and sh*Lrrk2* + Phospho-mimetic Ezrin O/E (p > 0.9999, 95% C.I. = [-3.589, 1.545]),
830 alpha = 0.05. Data points are mouse averages. (G) Quantification of astrocyte branching
831 complexity. n = 16 (shControl), 22 (shControl + Phospho-mimetic Ezrin O/E), 21 (sh*Lrrk2*),
832 21 (sh*Lrrk2* + Phospho-mimetic Ezrin O/E). Two-way ANOVA for repeated measures.
833 Main effects of conditions [F (2.435, 7008) = 225.0, p < 0.0001] and radius [F (88, 8633)

834 = 325.4, $p < 0.0001$] and interaction [F (264, 8633) = 5.908, $p < 0.0001$]. Bonferroni
835 multiple comparisons revealed a significant difference between shControl and sh*Lrrk2* (p
836 < 0.0001, 95% C.I. = [31.02, 40.20]), between sh*Lrrk2* and shControl + Phospho-mimetic
837 Ezrin O/E ($p < 0.0001$, 95% C.I. = [-38.59, -29.67]), between sh*Lrrk2* and sh*Lrrk2* +
838 Phospho-mimetic Ezrin O/E ($p < 0.0001$, 95% C.I. = [-34.32, -25.69]), between shControl
839 and sh*Lrrk2* + Phospho-mimetic Ezrin O/E ($p = 0.0139$, 95% C.I. = [0.7510, 10.47]), and
840 between shControl + Phospho-mimetic Ezrin O/E and sh*Lrrk2* + Phospho-mimetic Ezrin
841 O/E ($p = 0.0188$, 95% C.I. = [0.4426, 7.813]), and no difference between shControl and
842 shControl + Phospho-mimetic Ezrin O/E ($p > 0.9999$, 95% C.I. = [-3.083, 6.044]). Data
843 are presented as mean ± s.e.m.

844 **Figure 6: LRRK2 G2019S alters the interactome of astrocytic Ezrin *in vivo*.** (A)
845 astrocyte-specific AAVs (serotype PHP.eB) were used to express Ezrin or nonspecific
846 cytosolic control. NES, nuclear export sequence; ITR, inverted terminal repeats;
847 GfaABC1D truncated GFAP promoter; HA, hemagglutinin tag; pA, polyadenylation. (B)
848 outline of the experimental paradigm. n = 3 biological replicates per construct per
849 genotype (1 replicate = 2 animals per pooled sample). (C) Volcano plot showing the
850 differential abundance of proteins detected by Astro-Ezrin-BioID in WT and LRRK2
851 G2019S$^{ki/ki}$ cortices. (D-E) Bars show the top 10 most significant Gene Ontology (GO)
852 terms, ordered by lowest adjusted p-value, for the proteins differentially detected by Astro-
853 Ezrin-BioID in WT compared to LRRK2 G2019S$^{ki/ki}$ (D) Molecular function (E) Biological
854 Process. (F) The interaction network depicts 58 high-confidence proteins that gained or
855 lost proximity to Ezrin in LRRK2 G2019S$^{ki/ki}$ compared to WT mice. (G-H) heatmaps depict

856 fold-change in abundance (Astro-Ezrin-BioID / Asto-Cyto-BioID) of proteins with high
857 confidence changed proximity to Ezrin in LRRK2 G2019S$^{ki/ki}$ astrocytes.

858 **Figure 7: Interaction Between Atg7 and Ezrin Depends on Ezrin's Phosphorylation**
859 **State.** (A) Schematic of domains within Atg7. (B) Predicted model of Atg7 homodimer. (C)
860 Schematic of domains within Ezrin. (D) Model of the predicted structure of Ezrin in its
861 closed or open conformation. (E) Model of the predicted interaction between Atg7
862 homodimer and Ezrin. (F) (Upper) Model of the predicted structural changes of Ezrin
863 when bound to Atg7. (Lower) Model of the predicted structural changes of Atg7 when
864 bound to Ezrin. (G) Co-immunoprecipitation of Ezrin-HA by Atg7-Myc pull down.
865 Immunoblot of HEK293T cell lysates overexpressing WT Ezrin, phospho-dead Ezrin, or
866 phospho-mimetic Ezrin with or without Atg7-Myc. Ezrin is detected by an anti-HA antibody,
867 while Atg7 is detected by an anti-Myc antibody. (H) Quantification of Ezrin co-
868 immunoprecipitation signal intensity in (G). Signals corresponding to Ezrin were first
869 normalized to that for WT Ezrin. Statistical significance was determined by One-way
870 ANOVA [F (2, 6) = 9.932, p = 0.0125]. Tukey's multiple comparisons test revealed a
871 significant difference between WT Ezrin and phospho-mimetic Ezrin (p = 0.0151, 95% C.I.
872 = [0.1724, 1.205]) and between phospho-dead Ezrin and phospho-mimetic Ezrin (p =
873 0.0272, 95% C.I. = [0.08525, 1.118]) and no differences between WT Ezrin and phospho-
874 dead Ezrin (p = 0.8658, 95% C.I. = [-0.4292, 0.6035]), alpha = 0.05. n = 3 independent
875 experiments. (I) Images of ACC and MOp L2-3 WT and LRRK2 G2019S$^{ki/ki}$ astrocytes at
876 P21 expressing shControl-PB-mCherry-CAAX or sh*Atg7*-PB-mCherry-CAAX. Astrocyte
877 territory in cyan. Scale bar, 10 µm. (J) Average territory volumes of P21 astrocytes. n =
878 20 (WT shControl; 4 mice), 21 (WT sh*Atg7*; 4 mice), 25 (LRRK2 G2019S$^{ki/ki}$ shControl; 5

879 mice), 23 (LRRK2 G2019S$^{ki/ki}$ sh*Atg7*; 5 mice). Statistical significance was determined by
880 Nested one-way ANOVA [F (3, 28) = 9.484, p = 0.0002]. Bonferroni multiple comparisons
881 revealed a significant difference between WT shControl and LRRK2 G2019S$^{ki/ki}$ shControl
882 (p = 0.0036, 95% C.I. = [0.4504, 2.701]), between WT shControl and WT sh*Atg7* (p =
883 0.0003, 95% C.I. = [0.8655, 3.176]), and between WT sh*Atg7* and LRRK2 G2019S$^{ki/ki}$
884 sh*Atg7* (p = 0.0109, 95% C.I. = [-2.502, -0.2662]), and no differences between WT
885 shControl and LRRK2 G2019S$^{ki/ki}$ sh*Atg7* (p = 0.4294, 95% C.I. = [-0.4935, 1.766]),
886 between LRRK2 G2019S$^{ki/ki}$ shControl and WT sh*Atg7* (p = 0.6977, 95% C.I. = [-0.6684,
887 1.558]), and between LRRK2 G2019S$^{ki/ki}$ shControl and LRRK2 G2019S$^{ki/ki}$ sh*Atg7* (p =
888 0.1089, 95% C.I. = [-2.026, 0.1480]), alpha = 0.05. Data points are mouse averages. (K)
889 Quantification of astrocyte branching complexity. n = 20 (WT shControl; 4 mice), 21 (WT
890 sh*Atg7*; 4 mice), 26 (LRRK2 G2019S$^{ki/ki}$ shControl; 5 mice), 23 (LRRK2 G2019S$^{ki/ki}$
891 sh*Atg7*; 5 mice). Two-way ANOVA for repeated measures. Main effects of conditions [F
892 (2.324, 472.6) = 43.1, $p < 0.05$] and radius [F (9, 250) = 301.8, $p < 0.05$] and interaction
893 [F (27, 610) = 4.539, $p < 0.05$]. Bonferroni multiple comparisons revealed a significant
894 difference between WT shControl and LRRK2 G2019S$^{ki/ki}$ shControl ($p < 0.0001$, 95% C.I.
895 = [34.87, 66.02]), between WT shControl and WT sh*Atg7* ($p < 0.0001$, 95% C.I. = [26.39,
896 58.96]), between WT shControl and LRRK2 G2019S$^{ki/ki}$ sh*Atg7* (p = 0.0021, 95% C.I. =
897 [6.359, 41.23]), between LRRK2 G2019S$^{ki/ki}$ shControl and LRRK2 G2019S$^{ki/ki}$ sh*Atg7* (p
898 < 0.0001, 95% C.I. = [-36.99, -16.31]), and between WT sh*Atg7* and LRRK2 G2019S$^{ki/ki}$
899 sh*Atg7* (p = 0.0006, 95% C.I. = [-31.62, -6.15]), and no difference between LRRK2
900 G2019S$^{ki/ki}$ shControl and WT sh*Atg7* (p = 0.3353, 95% C.I. = [-18.53, 2.994]).

901 **STAR METHODS**

902 **KEY RESOURCES TABLE**

REAGENT or RESOURCE	SOURCE	IDENTIFIER
β-actin	Sigma-Aldrich	Cat# A5441, RRID: AB_476744
ERM	Cell Signaling	Cat# 3142, RRID:AB_2100313
GAPDH	Abcam	Cat# ab8245, RRID:AB_2107448
Gephyrin	Synaptic Systems	Cat# 147 011, RRID:AB_887717
GFAP	Agilent	Cat# Z0334, RRID:AB_10013382
GFAP	Millipore	Cat# AB5541, RRID:AB_177521
GFP	Aves labs	GFP-1020, RRID:AB_10000240
HA	Roche	Cat# 11867423001, RRID:AB_390918
L1 (ASCS4)	DSHB	Cat# ascs4, RRID:AB_528349
LRRK2	Abcam	Cat# ab133474, RRID:AB_2713963
phospho-ERM	Cell Signaling	Cat# 3141, RRID:AB_330232
phospho-ERM	Cell Signaling	Cat# 3726, RRID: AB_10560513
phospho-Rab10	Abcam	Cat# ab230261, RRID:AB_2811274
PSD-95	Innovative Research	Cat# 51-6900, RRID: AB_87705
Sox9	Millipore	Cat# AB5535, RRID:AB_2239761
VGAT	Synaptic Systems	Cat# 131 004, RRID: AB_887873
VGluT1	Synaptic Systems	Cat# 135304, RRID: AB_887878
Bacterial and virus strains		
One Shot STBL3	Thermo Fisher	Cat# C737303
AAV PhP.eB	This paper	N/A
Chemicals, peptides, and recombinant proteins		
AraC	Sigma	Cat# C1768
B27	GIBCO	Cat# 17504044
B27 Plus	GIBCO	Cat# A3582801
BDNF	PeproTech	Cat# 450-02
Carboxypeptidase E	R&D	Cat# 3587-ZN
CNTF	PeproTech	Cat# 450-13
DMEM	GIBCO	Cat# 11960
DPBS	GIBCO	Cat# 14287
Dystroglycan	R&D	Cat# 6868-DG
Fetal Bovine Serum	Thermo Fisher	Cat# 10-437-028

Forskolin	Sigma	Cat# F6886
Glycerol	Acros Organics	Cat# AC158920010
L-Glutamine	GIBCO	Cat# 25030-081
Hydrocortisone	Sigma	Cat# H0888-5G
Insulin	Sigma	Cat# I1882
Neurobasal	GIBCO	Cat# 21103049
Neurobasal Plus	GIBCO	Cat# A3582901
Odyssey Blocking Buffer	LI-COR Biosciences	Cat# 927-40000
Opti-MEM	Thermo Fisher	Cat# 11058021
Paraformaldehyde	Electron microscopy Sciences	Cat# 19210
Pen/Strep	GIBCO	Cat# 15140
PhosSTOP™	Roche	Cat# 4906845001
Poly-D-Lysine	Sigma	Cat# P6407
Protease Inhibitor Cocktail	Roche	Cat# 4693132001
RIPA Buffer	Sigma	Cat# R0278
Sodium Pyruvate	GIBCO	Cat# 11360-070
Tissue-Tek® O.C.T. Compound	Sakura® Finetek	Cat# 4583
Triton X-100	Roche	Cat# 11332481001
Critical commercial assays		
Endo-Free Maxi Prep Kit	QIAGEN	Cat# 12362
Experimental models: cell lines		
HEK293T	ATCC	CRL-11268
Rat primary cortical neurons	This paper	N/A
Rat primary cortical astrocytes	This paper	N/A
Experimental models: organisms/strains		
Mouse: Aldh1L1-EGFP	MMRRC	RRID: MMRRC_011015-UCD
Mouse: CD1	Charles River	RRID: IMSR_CRL:022

Mouse: LRRK2 G2019S$^{ki/ki}$	Taconic	RRID: IMSR_TAC:13940
Rat: Sprague-Dawley	Charles River	001
Recombinant DNA		
pZac2.1-GfaABC1D-Ezrin WT-BioID2-HA	This paper	N/A
pZac2.1-GfaABC1D-Ezrin T567D-BioID2-HA	This paper	N/A
pZac2.1-GfaABC1D-Ezrin T567A-BioID2-HA plasmid	This paper	N/A
pLKO.1-sh*Atg7*-EGFP	This paper	N/A
pLKO.1-shControl-EGFP	This paper	N/A
pPB-CAG-sh*LRRK2*-mCherry-CAAX	This paper	N/A
pPB-CAG-sh*Atg7*-mCherry-CAAX	This paper	N/A
pPB-CAG-shControl-mCherry-CAAX	This paper	N/A
Software and algorithms		
GraphPad Prism 9	GraphPAD	https://www.graphpad.com/scientific-software/prism/
ImageJ	NIH	https://imagej.nih.gov/ij/
Puncta Analyzer	Savage et al., 2024[91]	https://github.com/Eroglu-Lab/Syn_Bot
Minhee Analysis	Kim et al., 2021[92]	https://github.com/parkgilbong/Minhee_Analysis_Pack
In vitro Sholl analysis	Tan et al., 2023[93]	https://github.com/Eroglu-Lab/In-Vitro-Sholl
Image Studio	LICOR	https://www.licor.com

903

904 **RESOURCE AVAILABILITY**

905 **Lead contact**

906 Further information and requests for resources and reagents should be directed to and
907 will be fulfilled by the lead contacts, Shiyi Wang (shiyi.wang@duke.edu) and Cagla Eroglu
908 (cagla.eroglu@duke.edu).

909 **Materials availability**

910 The reagents generated in this study are available without restriction.

911 **Data and code availability**

912 The data generated during this study are available from the lead contact upon request.
913 The proteomic data is uploaded in the repository Massive (massive.ucsd.edu), accession
914 number: MSV000095133

915 **EXPERIMENTAL MODELS AND SUBJECT DETAILS**

916 **Animals**

917 All mice and rats were used in accordance with the Institutional Animal Care and Use
918 Committee (IACUC) and the Duke Division of Laboratory Animal Resources (DLAR)
919 oversight (IACUC Protocol Numbers A147-17-06 and A117-20-05). All mice and rats were
920 housed under typical day/night conditions of 12-hour cycles. LRRK2 G2019S$^{ki/ki}$ mice
921 (RRID: IMSR_TAC:13940) were obtained through Taconic. This model was generated on
922 the C57BL6/NTac background. It has been maintained on that pure background in
923 Taconic. Aldh1l1-EGFP (RRID: MMRRC_011015-UCD) mice were obtained through
924 MMRRC and backcrossed on a C57BL/6J background. Wild-type CD1 mice used for
925 PALE were purchased through Charles River Laboratories (RRID: IMSR_CRL:022).

926 Mice and rats were used for experiments as specified in the text and figure legends.
927 For all experiments, age, and sex-matched mice were randomly assigned to experimental

928 groups based on genotypes. Mice of both sexes were included in the analysis, and we
929 did not observe any influence or association of sex on the experimental outcomes.

930 **Primary cortical neuron isolation and culture**

931 Purified (glia-free) rat cortical neurons were prepared as described previously[40]. Briefly,
932 cortices from P1 rat pups of both sexes (Sprague Dawley, Charles River Laboratories,
933 SD-001) were micro-dissected, digested in papain (~7.5 units/ml) at 33°C for 45 minutes,
934 triturated in low and high ovomucoid solutions, resuspended in panning buffer (DPBS
935 (GIBCO 14287) supplemented with BSA and insulin) and passed through a 20 µm mesh
936 filter (Elko Filtering 03-20/14). Filtered cells were incubated on negative panning dishes
937 coated with Bandeiraea Simplicifolia Lectin 1 (x2), followed by goat anti-mouse IgG+IgM
938 (H+L) (Jackson ImmunoResearch 115-005-044), and goat anti-rat IgG+IgM (H+L)
939 (Jackson ImmunoResearch 112-005-044) antibodies, then incubated on positive panning
940 dishes coated with mouse anti-L1 (ASCS4, Developmental Studies Hybridoma Bank,
941 Univ. Iowa) to bind cortical neurons. Adherent cells were collected by forceful pipetting
942 with a P1000 pipette. Isolated neurons were pelleted (11 minutes at 200 g) and
943 resuspended in serum-free neuron growth media (NGM; Neurobasal, B27 supplement,
944 2 mM L-Glutamine, 100 U/ml Pen/Strep, 1 mM sodium pyruvate, 4.2 µg/ml Forskolin,
945 50 ng/mL BDNF, and 10 ng/mL CNTF). 70,000 neurons were plated onto 12 mm glass
946 coverslips coated with 10 µg/ml poly-D-lysine (PDL, Sigma P6407) and
947 2 µg/ml laminin and incubated at 37°C in 10% CO_2. On day *in-vitro* (DIV) 2, half of the
948 media was replaced with NGM Plus (Neurobasal Plus, B27 Plus, 100 U/mL Pen/Strep,
949 1 mM sodium pyruvate, 4.2 µg/ml Forskolin, 50 ng/ml, BDNF, and 10 ng/ml CNTF) and
950 AraC (10 µM) was added to stop the growth of proliferating contaminating cells. On DIV

951 3, all the media was replaced with NGM Plus. In experiments involving lentivirus infection,
952 100 µl of supernatant containing lentivirus plus polybrene (1 µg/ml) was added to the
953 AraC NGM mixture on DIV 2 and completely washed out on DIV 3 and replaced with NGM
954 Plus containing 100 ng/ml BDNF. Neurons were fed on DIV 6 and DIV 9 by replacing half
955 of the media with NGM Plus.

956 **Primary cortical astrocyte isolation and culture**

957 **Rat astrocyte isolation and culture**

958 Rat cortical astrocytes were prepared as described previously[40]. P1 rat cortices from both
959 sexes were micro-dissected, papain digested, triturated in low and high ovomucoid
960 solutions, and resuspended in astrocyte growth media (AGM: DMEM (GIBCO 11960), 10%
961 FBS, 10 µM, hydrocortisone, 100 U/ml Pen/Strep, 2 mM L-Glutamine, 5 µg/ml Insulin,
962 1 mM Na Pyruvate, 5 µg/ml N-Acetyl-L-cysteine). Between 15-20 million cells were plated
963 on 75 mm^2 flasks (non-ventilated cap) coated with poly-D-lysine and incubated at 37°C
964 in 10% CO_2. On DIV 3, the removal of non-astrocyte cells was performed by forcefully
965 shaking closed flasks by hand for 10-15 s until only an adherent monolayer of astrocytes
966 remained. AraC was added to the media from DIV 5 to DIV 7 to eliminate contaminating
967 fibroblasts. On DIV 7, astrocytes were trypsinized (0.05% Trypsin-EDTA) and plated into
968 12-well or 6-well dishes. On DIV 8, cultured rat astrocytes were transfected
969 with shRNA and/or expression plasmids using Lipofectamine LTX with Plus Reagent
970 (Thermo Scientific) per the manufacturer's protocol. Briefly, 1 µg (12-well) or 2 µg (6-well)
971 total DNA was diluted in Opti-MEM containing Plus Reagent, mixed with Opti-MEM
972 containing LTX (1:2 DNA to LTX), and incubated for 30 minutes. The transfection solution
973 was added to astrocyte cultures and incubated at 37°C for 3 hours. On DIV 10, astrocytes

974 were trypsinized, resuspended in NGM plus, plated (20,000 cells per well) onto DIV 10
975 neurons, and co-cultured for 48 hours.

976 **shRNA plasmids**

977 pLKO.1 Puro plasmids containing shRNA (pLKO.1-shRNA) against
978 mouse/rat *Lrrk2* (sh*Lrrk2*: TRCN0000322193; GGCCGAGTTGTGGATCATATT) and
979 mouse/rat *Atg7* (sh*Atg7*: TRCN0000092163; TATTATTGAGTTCAGAGCTGG), were
980 obtained from the RNAi Consortium (TRC) via Dharmacon. Two scrambled shRNA
981 sequences were generated (GTTGCTGAATGGCGGATCTAT;
982 GTTGCGGTTATGAATAGTACT) and cloned into the pLKO.1 TRC cloning vector[94]
983 according to Addgene protocols (https://www.addgene.org/protocols/plko/). To generate
984 pLKO.1 shRNA plasmids that express EGFP (pLKO.1-shRNA-EGFP), CAG-EGFP was
985 removed from pLenLox-shNL1-CAG-EGFP[95] and inserted between Kpn1 and SpeI sites
986 in pLKO.1 Puro, replacing the puromycin resistance gene. pLKO.1 shRNA mCherry
987 plasmids were generated by replacing EGFP with mCherry between KpnI and NheI sites.

988 **PiggyBac plasmids**

989 pPB-CAG-EGFP and pGLAST-PBase were a gift from Dr. Joseph Loturco[96]. To generate
990 pPB-CAG-mCherry-CAAX, mCherry-CAAX was inserted between XmaI and NotI
991 restrictions sites to replace EGFP. To insert the hU6 promoter and shRNA in pPB-CAG-
992 mCherry-CAAX, a DNA fragment containing hU6 and shRNA was amplified from pLKO.1-
993 shRNA using Phusion High-Fidelity DNA Polymerase (NEB) with primers that introduced
994 SpeI restriction sites (Forward Primer: GGACTAGTCAGGCCCGAAGGAATAGAAG;
995 Reverse Primer: GGACTAGTGCCAAAGTGGATCTCTGCTG). PCR products were

996 purified, digested with SpeI, and ligated into pPB-CAG-mCherry-CAAX at the SpeI
997 restriction site. An analytical digest with EcoRI followed by sequencing was used to
998 confirm the orientation of the inserted DNA fragment.

999 **Ezrin plasmids**

1000 pZac2.1-GfaABC1D-Lck-GCaMP6f was a gift from Dr. Baljit Khakh (Addgene plasmid
1001 #52924). pZac2.1-GfaABC1D-BioID2-HA was generated by PCR of BioID2 from pAAV-
1002 hSyn-BioID2-Linker-Synapsin1a-HA[97] (primers Fwd: 5'-
1003 ctagcctcgagaattcaccatgttcaaaaatcttatttg-3', Rev: 5'-
1004 ccgggtcgactctagatgcgtaatccggtacatcg-3') and insertion into the EcoRI and XbaI
1005 restriction sites of pZac2.1-GfaABC1D-Lck-GCaMP6f using In-Fusion cloning (TaKaRa).
1006 pHJ421(pEGFP-Ezrin WT) and pHJ423 (pEGFP-Ezrin T567D) were a gift from Stephen
1007 Shaw (Addgene plasmid # 20680 and # 20681). pZac2.1-GfaABC1D-Ezrin WT-BioID2-
1008 HA and pZac2.1-GfaABC1D-Ezrin T567D-BioID2-HA were generated by PCR of Ezrin
1009 from pHJ421 or pHJ423 (primers Fw: 5'-ctagcctcgagaattcaccatgccgaaaccaatca-3', Rv:
1010 5'-tgaacatggtgaattccgacagggcctcgaactcg-3') and insertion into the EcoRI restriction sites
1011 of pZac2.1-GfaABC1D-BioID2, respectively. To generate pZac2.1-GfaABC1D-Ezrin
1012 T567A-BioID2-HA plasmid, Q5® Site-Directed Mutagenesis Kit (NEB) was used with
1013 mutagenesis primers (Fwd: CAAGTACAAGGCGCTGCGGCAGA; Rev:
1014 TCCCGGCCTTGCCTCATG)

1015 **Lentivirus production and transduction**

1016 Lentiviruses containing shRNA targeting vectors were produced to test the knockdown
1017 efficiency of shRNA constructs in cultured primary astrocytes or to bulk transduce

1018 neurons with shRNA and GFP. To produce lentivirus, HEK293T cells were transfected
1019 with a pLKO.1 shRNA Puro targeting plasmid (for astrocyte transduction), an envelope
1020 plasmid (VSVG), and a packaging plasmid (dR8.91) using X-tremeGENE (Roche). One
1021 day after transfection, the media was replaced with AGM (for astrocyte transduction), and
1022 media containing lentivirus was collected on days 2 and 3 post-transfection. To assess
1023 the knockdown efficiency of shRNAs in astrocytes, rat primary astrocytes at DIV 7 were
1024 plated in 6-well dishes in 2 ml of AGM. On DIV 8, 1 ml of AGM was removed, and 500 µl
1025 of fresh AGM was added along with 500 µl of lentivirus-containing media and 1 µg/ml
1026 polybrene. Cultured astrocytes were treated with puromycin (1 µg/ml) from DIV 10-15 to
1027 select for transduced cells. Cultured astrocytes were lysed at DIV 15 for protein extraction
1028 and Western blot analysis.

1029 **Immunocytochemistry**

1030 Astrocyte-neuron co-cultures on glass coverslips were fixed on DIV 12 with warm 4%
1031 PFA for 7 minutes, washed 3 times with PBS, blocked in a blocking buffer containing 50%
1032 normal goat serum (NGS) and 0.4% Triton X-100 for 30 minutes, and washed in PBS.
1033 Samples were then incubated overnight at 4°C in primary antibodies diluted in blocking
1034 buffer containing 10% NGS, washed with PBS, incubated in Alexa Fluor conjugated
1035 secondary antibodies (Life Technologies) for 2 hours at room temperature, and washed
1036 again in PBS. Coverslips were mounted onto glass slides (VWR Scientific) with
1037 Vectashield mounting media containing DAPI (Vector Labs), sealed with nail polish, and
1038 imaged on an AxioImager M1 (Zeiss) fluorescence microscope. Images of healthy
1039 astrocytes with strong expression of fluorescent markers that did not overlap with other
1040 fluorescent astrocytes were acquired at 40x magnification in red, green, and/or DAPI

1041 channels using a CCD camera. Astrocyte morphological complexity was analyzed in FIJI
1042 using the Sholl analysis plugin[98], as described previously[40] (https://github.com/Eroglu-
1043 Lab/In-Vitro-Sholl). Statistical analyses were conducted using a custom code in R
1044 (https://github.com/Eroglu-Lab/In-Vitro-Sholl). A mixed-effect model with multiple
1045 comparisons made using the Tukey post-test was used for Sholl analysis to account for
1046 the variability per experiment as a random effect to evaluate differences between the
1047 conditions. The exact number of independent experiments and the exact number of cells
1048 analyzed are indicated in the figure legend for each experiment. To ensure the health of
1049 astrocyte-neuron co-cultures, the peak for the number of astrocyte intersections must be
1050 greater than or equal to 25 in the control condition. We imaged non-overlapping
1051 astrocytes that contained a single nucleus (DAPI stain) and expressed consistent
1052 fluorescent markers and Ezrin constructs according to the experimental conditions.

1053 **Postnatal astrocyte labeling by electroporation (PALE)**

1054 Late P0/early P1 mice were sedated by hypothermia until anesthetized, and 1 µl
1055 of plasmid DNA mixed with Fast Green Dye was injected into the lateral ventricle of one
1056 hemisphere using a pulled glass pipette (Drummond). For shRNA knockdown
1057 experiments in wild-type CD1 mice, the 1 µl of DNA contained 1 µg of pGLAST-PBase
1058 and 1 µg of pPB-shRNA-mCherryCAAX was injected. To label astrocytes in WT
1059 and LRRK2 G2019S$^{ki/ki}$ mice, the 1 µl of DNA contained 1 µg of pGLAST-PBase and 1
1060 µg of pPB-mCherry-CAAX was injected per mouse.

1061 For PALE-mediated overexpression of phospho-mimetic Ezrin in shRNA knockdown
1062 experiments, 0.5 µg pGLAST-PBase, 0.5 µg pPB-shRNA-mCherryCAAX, and 1 µg
1063 pZac2.1-GfaABC1D-Ezrin T567D-BioID2-HA were injected in a total volume of 1 µl. For

1064 phospho-dead Ezrin overexpression in WT and LRRK2 G2019S$^{ki/ki}$ mice, 0.5 μg pGLAST-
1065 PBase, 0.5 μg of pZac2.1-gfaABC1D-mCherry-CAAX and 1 μg of pZac2.1-GfaABC1D-
1066 Ezrin T567A-BioID2-HA were injected in a total volume of 1 μl. Following DNA injection,
1067 electrodes were oriented with the positive terminal above the frontal cortex and the
1068 negative terminal below the chin, and 5 discrete 50 ms pulses of 100 V spaced 950 ms
1069 apart were applied. Pups were recovered on a heating pad, returned to their home cage,
1070 and monitored until collection at P21. The number of mice used for each experiment is
1071 indicated in the figure legends. All animals appeared healthy at the time of collection.
1072 Brain sections were examined for the presence of electroporated cells before staining.

1073 **Adeno-associated virus (AAV) production and administration**

1074 Purified AAVs were produced as described previously[99]. Briefly, HEK293T cells were
1075 transfected with pAd-DELTA F6, serotype plasmid AAV PHP.eB, and AAV plasmid
1076 (pZac2.1-GfaABC1D-Ezrin-BioID2-HA or pZac2.1-GfaABC1D-Ezrin T567A-BioID2-HA).
1077 Three days after transfection, cells were collected in 15 mM NaCl, 5 mM Tris-HCl, pH 8.5,
1078 and lysed with repeat freeze-thaw cycles followed by treatment with Benzonase (Novagen
1079 70664) at 37°C for 30 minutes. Lysed cells were pelleted by centrifugation, and the
1080 supernatant, containing AAVs, was applied to an Optiprep density gradient (Sigma D1556,
1081 15%, 25%, 40%, and 60%) and centrifuged at 67,000 rpm using a Beckman Ti-70 rotor
1082 for 1 hour. The AAV-enriched fraction was isolated from between 40% and
1083 60% iodixanol solution and concentrated by repeated washes with sterile PBS in an
1084 Amicon Ultra-15 filtration unit (NMWL: 100 kDa, Millipore UFC910008) to a final volume
1085 of ~100 μl and aliquoted for storage at −80°C. 9-week-old WT or LRRK2 G2019S$^{ki/ki}$ mice
1086 placed in a stereotaxic frame were anesthetized through inhalation of 1.5% isofluorane

1087 gas. 10 µl of purified AAVs having a titer of ~1 x 10^{12} GC/ml was introduced into the
1088 mouse brain intravenously by injection into the retro-orbital sinus. After 3 weeks at 12-
1089 week-old, mice were anesthetized with 200 mg/kg Tribromoethanol (Avertin) and
1090 transcardially perfused with TBS/Heparin and 4% paraformaldehyde (PFA) at room
1091 temperature (RT). Harvested brains were post-fixed overnight in 4% PFA, cryoprotected
1092 in 30% sucrose, and the brain blocks were prepared with O.C.T. (TissueTek) to store at
1093 −80°C. 30 µm thick brain sections were obtained through cryosectioning using a Leica
1094 CM3050S (Leica, Germany) vibratome and stored in a mixture of TBS and glycerol at
1095 −20°C for further free-float antibody staining procedures.

1096 **Immunohistochemistry on mouse brain sections**

1097 Mice used for immunohistochemistry were anesthetized with 200 mg/kg Avertin and
1098 perfused with TBS/Heparin and 4% PFA. Brains were collected and post-fixed in 4% PFA
1099 overnight, cryoprotected in 30% sucrose, frozen in a solution containing 2 parts 30%
1100 sucrose and 1-part O.C.T. (TissueTek), and stored at −80°C. Floating coronal tissue
1101 sections of 30 µm, 40 µm or 100 µm thickness were collected and stored in a 1:1 mixture
1102 of TBS/glycerol at −20°C. For immunostaining, sections were washed in 1x TBS
1103 containing 0.2% Triton X-100 (TBST), blocked in 10% NGS diluted in TBST, and
1104 incubated in primary antibody for 2-3 nights at 4°C with gentle shaking. Primary antibodies
1105 used were anti-LRRK2 (Rabbit, 1:500; ab133474, Abcam), HA (Rat, 1:500; 11867423001,
1106 Roche), phospho-ERM (Rabbit, 1:500; 3141, Cell Signaling), Sox9 (Rabbit, 1:500;
1107 AB5535, Millipore), GFAP (Rabbit, 1:500; Z0334, Agilent DAKO), VGluT1 (Guinea pig,
1108 1:2000; 135304, Synaptic Systems), PSD95 (Rabbit, 1:300; 51-6900, Innovative
1109 Research), VGAT (Guinea pig, 1:1000; 131004, Synaptic Systems), and Gephyrin

1110 (Rabbit, 1:1000; 147011, Synaptic Systems). Following the primary incubation, sections
1111 were washed in TBST, incubated in Alexa Fluor conjugated secondary antibodies diluted
1112 1:200 (Life Technologies) for 2-3 hours at room temperature, washed with TBST, and
1113 mounted onto glass slides using a homemade mounting media (90% Glycerol, 20 mM
1114 Tris pH 8.0, 0.5% n-Propyl gallate) and sealed with nail polish. For DAPI staining, DAPI
1115 (1:50,000) was added to the secondary antibody solution for the final 10 minutes of
1116 incubation. Images were acquired with an Olympus FV 3000 microscope.

1117 **Mouse astrocyte territory volume analysis**

1118 To assess the territory volume of individual astrocytes in the mouse cortex, 100 μm-thick
1119 floating sections containing anterior cingulate cortex (ACC) and primary motor cortex
1120 (MOp) astrocytes labeled sparsely via PALE with mCherry-CAAX were collected. High-
1121 magnification images containing an entire astrocyte (50-60 μm z-stack) were acquired
1122 with an Olympus FV 3000 microscope with the 60x objective. Criteria for data inclusion
1123 required that the entirety of the astrocyte could be captured within a single brain section
1124 and that the astrocyte was in L2-3 of the ACC or MOp. Astrocytes in which the entire
1125 astrocyte could not be captured within the section or was in other layers or outside of the
1126 ACC or MOp were not imaged. Imaged astrocytes were analyzed using Imaris Bitplane
1127 software as described previously[40]. Briefly, surface reconstructions were generated, and
1128 the Imaris Xtensions “Visualize Surface Spots” and “Convex Hull” were used to create an
1129 additional surface render representing the territory of the astrocyte. The volume of each
1130 territory was recorded, and astrocyte territory sizes from biological replicates were
1131 analyzed across experimental conditions using a nested two-way ANOVA followed by the
1132 Bonferroni posthoc test. For 3D Sholl analysis of individual PALE astrocytes, we first

1133 loaded images onto Imaris and then created a surface. After generating the surface of
1134 astrocytes, we created filaments using 'Add new filament (leaf icon)'. For the
1135 quantification of complexity, we clicked on the gear tool on Imaris to display Sholl
1136 intersections. The number of animals and cells/animals analyzed are specified in the
1137 figure legend for each experiment.

1138 **Biochemical assays**

1139 **mRNA extraction and cDNA preparation**

1140 Cells stored in TRIzol (15596026, Invitrogen) were thawed and resuspended in 1 mL of
1141 TRIzol. After adding 200 µL of chloroform, the samples were centrifuged at 12,000 g for
1142 15 minutes at 4°C. The aqueous phase was collected, and RNA was precipitated with
1143 GlycoBlue Coprecipitant (AM9515, Invitrogen) and isopropanol. The RNA pellet was
1144 washed with 75% ethanol, air-dried, and resuspended in 40 µL of nuclease-free water.
1145 The RNA was then isolated using the Zymo Research RNA Clean & Concentrator-5 Kit
1146 (R1014, Zymo), quantified with the Qubit RNA HS Assay Kit (Q32852, Invitrogen), and
1147 diluted to equalize concentrations. Finally, cDNA libraries were generated using qScript
1148 cDNA SuperMix (101414-102, VWR) with a temperature profile of 25°C for 5 minutes,
1149 42°C for 30 minutes, and 85°C for 5 minutes, and the resulting cDNA was diluted threefold
1150 and stored at −80°C.

1151 **Real-time qPCR**

1152 cDNA samples were plated on a 96-well qPCR plate and incubated with Fast SYBR
1153 Green Master Mix (4385616, Applied Biosystems), nuclease-free water, and the forward
1154 and reverse primers of interest at a ratio of 5 µl SYBR: 3 µl water: 0.5 µl forward primer:
1155 0.5 µl reverse primer: 1 µl sample. Each sample was plated two to four times to ensure

1156 technical replicates. A control sample (water with primers and Master Mix) served as a
1157 negative control. Cycle threshold values were collected for each well and normalized to
1158 GAPDH as a housekeeping gene. The sequences of forward (F) and reverse (R) primers
1159 used (5′→ 3′) are:

1160 Atg7: (F) 5′- GTTCGCCCCCTTTAATAGTGC -3′ and (R) 5′-
1161 TGAACTCCAACGTCAAGCGG -3′

1162 **Protein extraction and Western blotting**

1163 Protein was extracted from cultured rat astrocytes using membrane solubilization buffer
1164 (25 mM Tris pH 7.4, 150 mM NaCl, 1 mM $CaCl_2$, 1 mM $MgCl_2$, 0.5% NP-40, and protease
1165 inhibitors). Cultured astrocytes were washed twice with ice-cold TBS containing 1 mM
1166 $CaCl_2$ and 1 mM $MgCl_2$ and incubated on ice in membrane solubilization buffer for
1167 20 minutes with occasional agitation. Cell lysates were collected, vortexed briefly, and
1168 centrifuged at 4°C at high speed for 10 minutes to pellet non-solubilized material. The
1169 supernatant was collected and stored at −80°C.

1170 Pierce BCA Protein Assay Kit (Thermo Fisher) was used to determine protein
1171 concentration, and lysates were mixed with 4x Pierce™ Reducing Sample Buffer (Thermo
1172 Scientific) and incubated at 45°C for 45 minutes to denature proteins. 7-10 µg (cultured
1173 astrocyte lysates) of protein was loaded into Bolt™ 4–12% Bus-Tris Plus gels (Thermo
1174 Scientific) and run at 150 V for 1 hour. Proteins were transferred at 100 V to PVDF
1175 membrane (Millipore) for 1.5 hours, blocked in 5% BSA in TBST (137 mM NaCl, 2.68 mM
1176 KCl, 24.7 mM Tris-Base, 0.1% (w/v) Tween 20) for 1 hour and incubated in primary
1177 antibodies overnight at 4°C. Primary antibodies used were: anti-LRRK2 (Rabbit, 1:500;

1178 ab133474, abcam), GAPDH (mouse, 1:5000; ab8245, abcam), β-actin (mouse, 1:5000;
1179 A5441, Millipore Sigma). The next day, membranes were washed with TBST, incubated
1180 in HRP secondary antibodies (Thermo Fisher Scientific) for 2 hours, washed in TBST,
1181 and imaged on a Biorad Gel Doc imaging system. Protein levels were quantified using
1182 FIJI.

1183 **Coimmunoprecipitation**

1184 Co-immunoprecipitation assays were performed in HEK293T cells. Cells were
1185 transfected 36 hours prior to lysis with Ezrin/Atg7 cDNA using X-tremeGENE HP (Roche)
1186 and grown to 85-90% confluency. At 36 hours post-transfection, cells were rinsed with 1x
1187 PBS and collected for lysis. Cellular lysis and protein extraction was conducted via brief
1188 vortexing in chilled membrane solubilization buffer (25mM HEPES, 150mM KCl, 1.5mM
1189 MgCl2, 0.5% NP40, 10% Glycerol) in the presence of both protease (cOmplete, Roche)
1190 and phosphatase (PhosSTOP, Roche) inhibitors. Protein concentrations of cell lysates
1191 were equalized using the Pierce™ BSA Protein Assay Kit (Thermo Fisher) and
1192 CLARIOstar Plus Plate Reader (BMG Labtech). Equalized cell lysates were incubated,
1193 while rotating, with Pierce™ Anti-c-Myc Magnetic Beads (Thermo Fisher) for 6 hours at
1194 4°C. Following this incubation, the beads were washed with chilled lysis buffer. Protein
1195 samples were eluted from beads through the addition of 2x Bromophenol Blue-free
1196 Laemilli Sample Buffer and heating to 95°C for 5 minutes. Eluted protein samples were
1197 subjected to western blot analysis and quantification using a SimpleWestern Jess
1198 (ProteinSimple) automated immunoassay system with a 12-230kDa Fluorescence
1199 Separation module and associated manufacturer's protocol. Primary antibodies used for
1200 protein detection were: Anti-Myc (Rabbit, 1:40, Cell Signaling Technologies, mAb#2278)

1201 and Anti-HA (Rat, 1:20, Roche, 11867423001). Signal detection was achieved using the
1202 following fluorescently conjugated secondary antibodies at a dilution of 1:100: IRDye®
1203 680RD Goat anti-Rabbit IgG (LI-COR, 926-68071) and IRDye® 680RD Goat anti-Rat IgG
1204 (LI-COR, 926-68076). Signal quantification was conducted with the Simple Western
1205 Compass software, utilizing quantitative electropherograms of detected signals. Ezrin co-
1206 immunoprecipitation signal intensity was background-subtracted and normalized to Ezrin
1207 protein load and Atg7 IP levels for statistical analysis. Statistical analysis was performed
1208 in GraphPad Prism 9, using One-way ANOVA with Tukey's multiple comparisons test and
1209 alpha threshold of 0.05.

1210 **Protein interaction modeling**

1211 Full-length mouse Ezrin (UniProt ID: Q4KML7) and Atg7 (UniProt ID: Q9D906) were used
1212 for structure prediction in Alphafold 2.0 Multimer. The structure of Ezrin in the open
1213 conformation was generated by segmenting independently predicted Ezrin N- and C-
1214 termini and threading them onto an open ERM hinge structure using the PyMOL2
1215 molecular visualization software. To model the Ezrin:Atg7 interaction and associated
1216 conformational changes, the structures of Ezrin and the Atg7 homodimer were predicted
1217 and docked using Alphafold 2.0 Multimer. Conformational changes in the Ezrin:Atg7
1218 protein complex were assessed using PyMOL2 and CABS-flex 2.0[100]. For all predicted
1219 structure models, the highest-confidence structures, calculated via the predicted local
1220 distance difference test (pLDDT), were subjected to energy-minimization via AMBER
1221 relaxation. The resulting minimized structures were imported into PyMOL2 for
1222 representative model production.

1223 **Proteomic analysis**

1224 ***In vivo* BioID protein purification**

1225 *In vivo,* BioID experiments were performed as previously described in Takano et al., 2020
1226 with modifications[101]. Genotype-matched animals (wild-type C57BL6 or LRRK2
1227 G2019S$^{ki/ki}$) were bred to produce single-genotype litters. For each genotype (WT or
1228 G2019S), 6 pups were injected with AAVs carrying Astro-Ezrin-BioID
1229 (PHP.eB.GfaABC1D-Ezrin WT-BioID2-HA) or Astro-CYTO-BioID (PHP.eB.GfaABC1D-
1230 BioID2-HA). 2 genotype-matched cortices were pooled at the time of protein isolation,
1231 yielding 3 independent replicates per BioID construct. 12 total samples (3 per genotype
1232 per construct) were subjected to LC-MS/MS and downstream analysis. WT and LRRK2
1233 G2019S$^{ki/ki}$ P0 – P2 mouse pups were anesthetized by hypothermia, and 1µl of each
1234 concentrated AAV-BioID vector was injected bilaterally into the cortex using a Hamilton
1235 syringe. Pups were monitored until they recovered on a heating pad. At P18, P19, and
1236 P20, biotin was subcutaneously injected at 24 mg/kg to increase the biotinylation
1237 efficiency. At P21, the cerebral cortices were removed and stored at -80° C. For the
1238 protein purification, each cortex was lysed in a buffer containing 50 mM Tris/HCl, pH 7.5;
1239 150 mM NaCl; 1 mM EDTA; protease inhibitor mixture (Roche); and phosphatase inhibitor
1240 mixture (PhosSTOP, Roche). Next, an equal volume of buffer containing 50 mM Tris/HCl,
1241 pH 7.5; 150 mM NaCl; 1 mM EDTA; 0.4 % SDS; 2 % TritonX-100; 2 % deoxycholate;
1242 protease inhibitor mixture; and phosphatase inhibitor mixture was added to the samples,
1243 following by sonication and centrifugation at 15,000 g for 10 min. The remaining
1244 supernatant was ultracentrifuged at 100,000g for 30min at 4° C. Finally, SDS detergent
1245 was added to the samples and heated at 45 ° C for 45 min. After cooling on ice, each
1246 sample was incubated with High-Capacity Streptavidin Agarose beads (ThermoFisher) at

1247 4° C overnight. Following incubation, the beads were serially washed: 1) twice with a
1248 solution containing 2% SDS; 2) twice with a buffer 1% TritonX-100, 1% deoxycholate, 25
1249 mM LiCl; 3) twice with 1M NaCl, and finally, five times with 50 mM ammonium bicarbonate.
1250 The biotinylated proteins attached to the agarose beads were eluted in a buffer of 125
1251 mM Tris/HCl, pH6.8; 4 % SDS; 0.2 % β-mercaptoethanol; 20 % glycerol; 3 mM biotin at
1252 60°C for 15min.

1253 **Sample Preparation**

1254 The Duke Proteomics and Metabolomics Shared Resource (DPMSR) received 12
1255 samples (3 of each WT CYT, GS CYT, WT EZR, and GS EZR) which were kept at -80C
1256 until processing. Samples were spiked with undigested bovine casein at a total of either
1257 1 or 2 pmol as an internal quality control standard. Next, they were reduced for 15 min at
1258 80C, alkylated with 20 mM iodoacetamide for 30 min at room temperature, then
1259 supplemented with a final concentration of 1.2% phosphoric acid and 636 µl of S-Trap
1260 (Protifi) binding buffer (90% MeOH/100mM TEAB). Proteins were trapped on the S-Trap
1261 micro cartridge, digested using 20 ng/µL sequencing grade trypsin (Promega) for 1 hr at
1262 47C, and eluted using 50 mM TEAB, followed by 0.2% FA, and lastly using 50% ACN/0.2%
1263 FA. All samples were then lyophilized to dryness. Samples were resuspended in 12 µl of
1264 1% TFA/2% acetonitrile with 12.5 fmol/µl of yeast ADH. A study pool QC (SPQC) was
1265 created by combining equal volumes of each sample.

1266 **LC-MS/MS Analysis**

1267 Quantitative LC/MS/MS was performed on 3 µL of each sample, using an MClass UPLC
1268 system (Waters Corp) coupled to a Thermo Orbitrap Fusion Lumos high resolution

1269 accurate mass tandem mass spectrometer (Thermo) equipped with a FAIMSPro device
1270 via a nanoelectrospray ionization source. Briefly, the sample was first trapped on a
1271 Symmetry C18 20 mm × 180 µm trapping column (5 µl/min at 99.9/0.1 v/v
1272 water/acetonitrile), after which the analytical separation was performed using a 1.8 µm
1273 Acquity HSS T3 C18 75 µm × 250 mm column (Waters Corp.) with a 90-min linear
1274 gradient of 5 to 30% acetonitrile with 0.1% formic acid at a flow rate of 400
1275 nanoliters/minute (nL/min) with a column temperature of 55C. Data collection on the
1276 Fusion Lumos mass spectrometer was performed for three difference compensation
1277 voltages (-40v, -60v, -80v). Within each CV, a data-dependent acquisition (DDA) mode
1278 of acquisition with a r=120,000 (@ m/z 200) full MS scan from m/z 375 – 1500 with a
1279 target AGC value of 4e5 ions was performed. MS/MS scans with HCD settings of 30%
1280 were acquired in the linear ion trap in "rapid" mode with a target AGC value of 1e4 and
1281 max fill time of 35 ms. The total cycle time for each CV was 0.66s, with total cycle times
1282 of 2 sec between like full MS scans. A 20s dynamic exclusion was employed to increase
1283 the depth of coverage. The total analysis cycle time for each sample injection was
1284 approximately 2 hours.

1285 **Quantitative Data Analysis**

1286 Following 15 total UPLC-MS/MS analyses (excluding conditioning runs, but including 3
1287 replicate SPQC samples), data were imported into Proteome Discoverer 3.0 (Thermo
1288 Scientific Inc.) and individual LCMS data files were aligned based on the accurate mass
1289 and retention time of detected precursor ions ("features") using Minora Feature Detector
1290 algorithm in Proteome Discoverer. Relative peptide abundance was measured based on
1291 peak intensities of selected ion chromatograms of the aligned features across all runs.

1292 The MS/MS data was searched against the SwissProt *M. musculus* database, a common
1293 contaminant/spiked protein database (bovine albumin, bovine casein, yeast ADH, etc.),
1294 and an equal number of reversed-sequence "decoys" for false discovery rate
1295 determination. Sequest with INFERYS was utilized to produce fragment ion spectra and
1296 to perform the database searches. Database search parameters included fixed
1297 modification on Cys (carbamidomethyl) and variable modification on Met (oxidation).
1298 Search tolerances were 2ppm precursor and 0.8Da product ion with full trypsin enzyme
1299 rules. Peptide Validator and Protein FDR Validator nodes in Proteome Discoverer were
1300 used to annotate the data at a maximum 1% protein false discovery rate based on q-
1301 value calculations. Note that peptide homology was addressed using razor rules in which
1302 a peptide matched to multiple different proteins was exclusively assigned to the protein
1303 has more identified peptides. Protein homology was addressed by grouping proteins that
1304 had the same set of peptides to account for their identification. A master protein within a
1305 group was assigned based on % coverage.

1306 Prior to normalization, a filter was applied such that a peptide was removed if it was not
1307 measured at least twice across all samples and in at least 50% of the replicates in any
1308 one single group. After that filter, samples were total intensity normalized (total intensity
1309 of all peptides for a sample are summed and then normalized across all samples). Next,
1310 the following imputation strategy is applied to missing values. If less than half of the values
1311 are missing in a biological group, values are imputed with an intensity derived from a
1312 normal distribution of all values defined by measured values within the same intensity
1313 range (20 bins). If greater than half values are missing for a peptide in a group and a
1314 peptide intensity is > 5e6, then it was concluded that the peptide was misaligned and its

1315 measured intensity is set to 0. All remaining missing values are imputed with the lowest
1316 2% of all detected values. Peptide intensities were then subjected to a trimmed-mean
1317 normalization in which the top and bottom 10 percent of the signals were excluded, and
1318 the average of the remaining values was used to normalize across all samples. Lastly, all
1319 peptides belonging to the same protein were then summed into a single intensity. These
1320 normalized protein level intensities are what was used for the remainder of the analysis.

1321 To assess technical reproducibility, we calculated the % coefficient of variation (%CV) for
1322 each protein across 3 injections of an SPQC pool that were interspersed throughout the
1323 study (Table S4). The mean %CV of the SPQC pools was 11.7%, which is well within our
1324 expected analytical tolerances. To assess biological + technical variability, %CVs were
1325 measured for each protein across the individual groups which averaged 19.8%, which is
1326 also within our normal tolerances and indicated a reproducible IP and sample processing.

1327 As an initial statistical analysis, we calculated fold-changes between various sample
1328 groups based on the protein expression values and calculated two-tailed heteroscedastic
1329 t-test on log2-transformed data for this comparison. Those fold changes and p-values are
1330 presented for all proteins in Tables S5, S7, S9, and S10. False Discovery Rate (FDR)
1331 correction was performed using the Benjamini-Hochberg procedure, and these values are
1332 reported ("p.adjusted") in Tables S5, S7, S9, and S10. To optimize for discovery, we opted
1333 to use the less stringent parameter of unadjusted p-value for downstream analyses.
1334 Within supplemental tables, we have labeled proteins significantly more abundant ("Up",
1335 fold change >1.5 and unadjusted p-value <0.05), or less abundant ("Down", fold change
1336 >-1.5 and unadjusted p-value <0.05) in a particular genotype or BioID sample group.
1337 These annotated proteins were used for downstream analyses, including protein

1338 interaction networks using Cytoscape (v.3.9.1) and Gene Ontology (GO) enrichment
1339 analysis using the ClusterProfiler package for R, with all M. musculus genes as the
1340 reference background.

1341 **Mouse synapse imaging and analysis**

1342 Staining, image acquisition, and analysis of synaptic density were performed as described
1343 previously[102]. Synaptic staining was performed in coronal sections (30 µm thick)
1344 containing the ACC and MOp from WT and LRRK2 G2019S$^{ki/ki}$ mice. To label pre and
1345 postsynaptic proteins, the following antibody combinations were used: VGluT1 and
1346 PSD95 (excitatory, intracortical), VGAT, and GEPHYRIN (inhibitory). High magnification
1347 60x objective plus 1.64x optical zoom z-stack images containing 15 optical sections
1348 spaced 0.34 µm apart were obtained using an Olympus FV 3000 inverted confocal
1349 microscope. Each z-stack was converted into 5 maximum projection images (MPI), each
1350 corresponding to a 1 µm section of z plane, using FIJI. Synapses were identified by the
1351 colocalization of pre and postsynaptic puncta. The number of co-localized synaptic puncta
1352 of excitatory intracortical (VGluT1-PSD95) and inhibitory (VGAT-GEPHYRIN) synapses
1353 were obtained using the FIJI plugin Puncta Analyzer[47]. 15 MPIs were analyzed for each
1354 mouse (5 MPI/tissue section, 3 tissue sections/mouse). Between 4 and 5, age and sex-
1355 matched mice/genotype/condition were analyzed for each synaptic staining combination,
1356 as indicated in the figure legends. All animals appeared healthy at the time of collection.
1357 No data were excluded.

1358 **Cell counting, imaging, and analysis**

1359 Tile scan images containing the anterior cingulated cortex (ACC) and primary motor
1360 cortex (MOp) from P21 WT and LRRK2 G2019S$^{ki/ki}$; Aldh1l1-eGFP mice were acquired
1361 on a confocal Leica SP8 STED microscope using the galvo scanner and 20x objective.
1362 For ALDH1L1-EGFP and SOX9 double positive cell counting in the ACC and MOp, the
1363 cells labeled with ALDH1L1-EGFP and SOX9 were counted by hand using the cell
1364 counter tool in FIJI. 2-4 sections per brain from 3 sex and age-matched mice/genotype
1365 were analyzed.

1366 **Human brain section staining**

1367 Floating human frontal cortex sections of 40 µm thickness were obtained from Banner
1368 Sun Health Research Institute in Sun City, Arizona (4 control and 3 LRRK2 G2019S
1369 mutation carrier subjects). None of the control subjects had a history of dementia or
1370 neurological or psychiatric disorders at the time of death (See Supplemental Table 1).
1371 Informed and written consent was obtained from the donors. For immunostaining,
1372 sections were washed in 1x TBS containing 0.3% Triton X-100 (TBST), blocked in 3%
1373 NGS diluted in TBST, and incubated in primary antibody 2-3 nights at 4°C with shaking.
1374 Primary antibodies used were GFAP (chicken, 1:250; AB5541, Millipore Sigma) and
1375 phospho-ERM (Rabbit, 1:250; #3726, Cell Signaling). Following primary incubation,
1376 sections were washed in TBST, incubated in Alexa Fluor conjugated secondary
1377 antibodies diluted 1:200 (Life Technologies) for 2-3 hours at room temperature, washed
1378 with TBST, and mounted onto glass slides using a homemade mounting media (90%
1379 Glycerol, 20 mM Tris pH 8.0, 0.5% n-Propyl gallate) and sealed with nail polish.

1380 **Mouse brain slice electrophysiology**

1381 For whole-cell patch-clamp recordings, 3-4 mice of each genotype and condition were
1382 used for miniature excitatory postsynaptic current (mEPSC) and miniature inhibitory
1383 postsynaptic current (mIPSC) measurements. WT and *LRRK2* G2019S$^{ki/ki}$ mice of both
1384 sexes were anesthetized with 200 mg/kg tribromoethanol (avertin) and decapitated. After
1385 decapitation, the brains were immersed in ice-cold artificial cerebrospinal fluid (aCSF, in
1386 mM): 125 NaCl, 2.5 KCl, 3 mM $MgCl_2$, 0.1 mM $CaCl_2$, 10 glucose, 25 $NaHCO_3$, 1.25
1387 $NaHPO_4$, 0.4 L-ascorbic acid, and 2 Na-pyruvate, pH 7.3-7.4 (310 mOsmol). 350 µm thick
1388 coronal slices containing the ACC were obtained using a vibrating tissue slicer (Leica
1389 VT1200; Leica Biosystems). Slices were immediately transferred to standard aCSF (33°C,
1390 continuously bubbled with 95% O_2 – 5% CO_2) containing the same as the low-calcium
1391 aCSF but with 1 mM $MgCl_2$ and 1-2 mM $CaCl_2$. After 30-minute incubation at 33°C, slices
1392 were transferred to a holding chamber with the same extracellular buffer at room
1393 temperature (RT: ~25°C). Brain slices were visualized by an upright microscope (BX61WI,
1394 Olympus) through a 40x water-immersion objective equipped with infrared-differential
1395 interference contrast optics in combination with a digital camera (ODA-IR2000WCTRL).
1396 Patch-clamp recordings were performed by using an EPC 10 patch-clamp amplifier,
1397 controlled by Patchmaster Software (HEKA). Data were acquired at a sampling rate of 50
1398 kHz and low-pass filtered at 6 kHz.

1399 To measure mEPSCs, the internal solution contained the following (in mM): 125 K-
1400 gluconate, 10 NaCl, 10 HEPES, 0.2 EGTA, 4.5 MgATP, 0.3 NaGTP, and 10 Na-
1401 phosphocreatine, pH adjusted to 7.2 – 7.4 with KOH and osmolality set to ~ 300 mOsmol.
1402 mEPSCs were measured in the aCSF bath solution containing 1 µM tetrodotoxin and 50
1403 µM Picrotoxin at -70 mV in voltage-clamp mode. To measure mIPSCs, the internal

1404 solution contained the following (in mM): 77 K-gluconate, 77 KCl, 10 HEPES, 0.2 EGTA,
1405 4.5 MgATP, 0.3 NaGTP, and 10 Na-phosphocreatine, pH adjusted to 7.2 – 7.4 with KOH
1406 and osmolality set to ~ 300 mOsmol. mIPSCs were measured in the aCSF bath solution
1407 containing 1 μM tetrodotoxin and 10 μM 6-cyano-7-nitroquinoxaline-2,3-dione (CNQX),
1408 and 50 μM D-2-amino-5-phosphonopentanoate (D-AP5) at -70 mV in voltage-clamp
1409 mode. mEPSCs and mIPSCs recorded at -70 mV were detected using Minhee Analysis
1410 software (https://github.com/parkgilbong/Minhee_Analysis_Pack). To analyze the
1411 frequency, events were counted over 5 minutes of recording. To obtain the average
1412 events for each cell, at least 100 non-overlapping events were detected and averaged.
1413 The peak amplitude of the average mEPSCs was measured relative to the baseline
1414 current.

1415 **Quantification and statistical analysis**

1416 All statistical analyses were performed in GraphPad Prism 9. Exact value of n, what n
1417 represents, and specific statistical tests for each experiment are indicated in the figure
1418 legend for each experiment. All data are represented as mean ± standard error of the
1419 mean, and data points are shown where applicable. Exact *P*-values are listed in the figure
1420 for each experiment. Where indicated, the unpaired two-tailed t-tests were run using
1421 Welch`s correction, and a correction for multiple comparisons was applied using Hom-
1422 Sidak method with an alpha threshold of 0.05 for adjusted *P*-value. A Geisser-
1423 Greenhouse correction was used for both One-way and Two-way ANOVA analyses. For
1424 Sholl analysis, statistical analyses were conducted using a custom code in R
1425 (https://github.com/Eroglu-Lab/In-Vitro-Sholl). A mixed-effect model with multiple
1426 comparisons made using the Tukey post-test was used for Sholl analysis to account for

1427 the variability per experiment as a random effect to evaluate differences between the
1428 conditions. Sample sizes were determined based on previous experience for each
1429 experiment to yield high power to detect specific effects. No statistical methods were used
1430 to predetermine the sample size. All experimental animals that appeared healthy at the
1431 time of tissue collection were processed for data collection.

ACKNOWLEDGMENTS

We thank Drs. Amy Lee, Zhiyong Liu, Nicole Calakos, Katja Brose, and Andrew Singleton for critical feedback about the manuscript. We thank Adam Okinaga and Donna Porter for their excellent technical help. This work was supported by a Foerster Bernstein Women In STEM Postdoctoral Fellowship to SW, and a Chan Zuckerberg Initiative, Neurodegeneration Challenge Network Collaborative grant (DAF2018-191999 and DAF2021-237435) to CE and ARLS, and by the N.I.H. grants R35-NS122140 to A.R.L.S. and R01-NS102237 to CE, and by the Michael J. Fox Foundation for Parkinson's Research (MJFF) Astrocyte Biology in PD pilot grant (MJFF 17914 to CE and ARLS), and by the joint efforts of MJFF and the Aligning Science Across Parkinson's (ASAP) initiative. MJFF administers the grant [ASAP-020607 to CE and SHS] on behalf of ASAP and the Michael J Fox Foundation. Dr. Cagla Eroglu is an HHMI Investigator. We are grateful to the Banner Sun Health Research Institute Brain and Body Donation Program of Sun City, Arizona for the provision of human biological materials. The Brain and Body Donation Program has been supported by the National Institute of Neurological Disorders and Stroke (U24 NS072026 National Brain and Tissue Resource for Parkinson's Disease and Related Disorders), the National Institute on Aging (P30AG19610 and P30AG072980, Arizona Alzheimer's Disease Center), the Arizona Biomedical Research Commission contracts 4001, 0011, 05-901 and 1001 to the Arizona Parkinson's Disease Consortium and the Michael J. Fox Foundation for Parkinson's Research.

IP RIGHTS NOTICE

This article is subject to HHMI's Open Access to Publications policy. HHMI lab heads have previously granted a nonexclusive CC BY 4.0 license to the public and a sublicensable license to HHMI in their research articles. Pursuant to those licenses, the author-accepted manuscript of this article can be made freely available under a CC BY 4.0 license immediately upon publication.

AUTHOR CONTRIBUTIONS

Conceptualization, SW, ARLS, and CE; Methodology, SW, RB, GS, DSB, LV, KS, JM, CXT, TT, MPR, KD, SHS, and CE; Investigation, SW, RB, GS, and LV; Formal analysis, SW, RB, GS, and LV; Resources, CXT, MPR, and KS; Writing – original draft, SW and CE; Writing – Review & Editing, SW and CE; Funding Acquisition, SW, SHS, ARLS, and CE.

DECLARATION OF INTERESTS

The authors declare no competing interests.

DATA AVAILABILITY

The data that support the findings of this study are available from the corresponding author (Dr. Cagla Eroglu) upon request after the publication of this manuscript. The data include experiment records, raw data, and analysis. The authors confirm that all data underlying the findings will be made fully available without restriction upon publication.

CODE AVAILABILITY

The code used to analyze Sholl data is available on the link https://github.com/Eroglu-Lab/Sholl_Macro.

1476 **REFERENCE**

1477 1 Bloem, B. R., Okun, M. S. & Klein, C. Parkinson's disease. *Lancet* **397**, 2284-
1478 2303 (2021). https://doi.org:10.1016/S0140-6736(21)00218-X

1479 2 Maiti, P., Manna, J. & Dunbar, G. L. Current understanding of the molecular
1480 mechanisms in Parkinson's disease: Targets for potential treatments. *Transl*
1481 *Neurodegener* **6**, 28 (2017). https://doi.org:10.1186/s40035-017-0099-z

1482 3 Blesa, J., Foffani, G., Dehay, B., Bezard, E. & Obeso, J. A. Motor and non-motor
1483 circuit disturbances in early Parkinson disease: which happens first? *Nat Rev*
1484 *Neurosci* **23**, 115-128 (2022). https://doi.org:10.1038/s41583-021-00542-9

1485 4 Foffani, G. & Obeso, J. A. A Cortical Pathogenic Theory of Parkinson's Disease.
1486 *Neuron* **99**, 1116-1128 (2018). https://doi.org:10.1016/j.neuron.2018.07.028

1487 5 Bandres-Ciga, S., Diez-Fairen, M., Kim, J. J. & Singleton, A. B. Genetics of
1488 Parkinson's disease: An introspection of its journey towards precision medicine.
1489 *Neurobiol Dis* **137**, 104782 (2020). https://doi.org:10.1016/j.nbd.2020.104782

1490 6 Udayar, V., Chen, Y., Sidransky, E. & Jagasia, R. Lysosomal dysfunction in
1491 neurodegeneration: emerging concepts and methods. *Trends Neurosci* **45**, 184-
1492 199 (2022). https://doi.org:10.1016/j.tins.2021.12.004

1493 7 Digre, A. & Lindskog, C. The Human Protein Atlas-Spatial localization of the
1494 human proteome in health and disease. *Protein Sci* **30**, 218-233 (2021).
1495 https://doi.org:10.1002/pro.3987

1496 8 Torres-Ceja, B. & Olsen, M. L. A closer look at astrocyte morphology:
1497 Development, heterogeneity, and plasticity at astrocyte leaflets. *Curr Opin*
1498 *Neurobiol* **74**, 102550 (2022). https://doi.org:10.1016/j.conb.2022.102550

1499 9 Allen, N. J. & Lyons, D. A. Glia as architects of central nervous system formation
1500 and function. *Science* **362**, 181-185 (2018).
1501 https://doi.org:10.1126/science.aat0473
1502 10 Semyanov, A. & Verkhratsky, A. Astrocytic processes: from tripartite synapses to
1503 the active milieu. *Trends Neurosci* **44**, 781-792 (2021).
1504 https://doi.org:10.1016/j.tins.2021.07.006
1505 11 Allen, N. J. & Eroglu, C. Cell Biology of Astrocyte-Synapse Interactions. *Neuron*
1506 **96**, 697-708 (2017). https://doi.org:10.1016/j.neuron.2017.09.056
1507 12 Clavreul, S. *et al.* Cortical astrocytes develop in a plastic manner at both clonal
1508 and cellular levels. *Nat Commun* **10**, 4884 (2019).
1509 https://doi.org:10.1038/s41467-019-12791-5
1510 13 Farizatto, K. L. G. & Baldwin, K. T. Astrocyte-synapse interactions during brain
1511 development. *Curr Opin Neurobiol* **80**, 102704 (2023).
1512 https://doi.org:10.1016/j.conb.2023.102704
1513 14 Tan, C. X. & Eroglu, C. Cell adhesion molecules regulating astrocyte-neuron
1514 interactions. *Curr Opin Neurobiol* **69**, 170-177 (2021).
1515 https://doi.org:10.1016/j.conb.2021.03.015
1516 15 Holt, L. M. *et al.* Astrocyte morphogenesis is dependent on BDNF signaling via
1517 astrocytic TrkB.T1. *Elife* **8** (2019). https://doi.org:10.7554/eLife.44667
1518 16 Kam, T. I., Hinkle, J. T., Dawson, T. M. & Dawson, V. L. Microglia and astrocyte
1519 dysfunction in parkinson's disease. *Neurobiol Dis* **144**, 105028 (2020).
1520 https://doi.org:10.1016/j.nbd.2020.105028

1521 17 Brandebura, A. N., Paumier, A., Onur, T. S. & Allen, N. J. Astrocyte contribution
1522 to dysfunction, risk and progression in neurodegenerative disorders. *Nat Rev*
1523 *Neurosci* (2022). https://doi.org:10.1038/s41583-022-00641-1
1524 18 Kluss, J. H., Mamais, A. & Cookson, M. R. LRRK2 links genetic and sporadic
1525 Parkinson's disease. *Biochem Soc Trans* **47**, 651-661 (2019).
1526 https://doi.org:10.1042/BST20180462
1527 19 Taylor, M. & Alessi, D. R. Advances in elucidating the function of leucine-rich
1528 repeat protein kinase-2 in normal cells and Parkinson's disease. *Curr Opin Cell*
1529 *Biol* **63**, 102-113 (2020). https://doi.org:10.1016/j.ceb.2020.01.001
1530 20 Steger, M. *et al.* Systematic proteomic analysis of LRRK2-mediated Rab GTPase
1531 phosphorylation establishes a connection to ciliogenesis. *Elife* **6** (2017).
1532 https://doi.org:10.7554/eLife.31012
1533 21 Kalogeropulou, A. F. *et al.* P62/SQSTM1 is a novel leucine-rich repeat kinase 2
1534 (LRRK2) substrate that enhances neuronal toxicity. *Biochem J* **475**, 1271-1293
1535 (2018). https://doi.org:10.1042/BCJ20170699
1536 22 Dhekne, H. S. *et al.* A pathway for Parkinson's Disease LRRK2 kinase to block
1537 primary cilia and Sonic hedgehog signaling in the brain. *Elife* **7** (2018).
1538 https://doi.org:10.7554/eLife.40202
1539 23 Lara Ordonez, A. J. *et al.* RAB8, RAB10 and RILPL1 contribute to both LRRK2
1540 kinase-mediated centrosomal cohesion and ciliogenesis deficits. *Hum Mol Genet*
1541 **28**, 3552-3568 (2019). https://doi.org:10.1093/hmg/ddz201
1542 24 Gomez, R. C., Wawro, P., Lis, P., Alessi, D. R. & Pfeffer, S. R. Membrane
1543 association but not identity is required for LRRK2 activation and phosphorylation

1544 of Rab GTPases. *J Cell Biol* **218**, 4157-4170 (2019).
1545 https://doi.org:10.1083/jcb.201902184
1546 25 Takagawa, T. *et al.* An increase in LRRK2 suppresses autophagy and enhances
1547 Dectin-1-induced immunity in a mouse model of colitis. *Sci Transl Med* **10** (2018).
1548 https://doi.org:10.1126/scitranslmed.aan8162
1549 26 Gan, L., Cookson, M. R., Petrucelli, L. & La Spada, A. R. Converging pathways
1550 in neurodegeneration, from genetics to mechanisms. *Nat Neurosci* **21**, 1300-
1551 1309 (2018). https://doi.org:10.1038/s41593-018-0237-7
1552 27 Steger, M. *et al.* Phosphoproteomics reveals that Parkinson's disease kinase
1553 LRRK2 regulates a subset of Rab GTPases. *Elife* **5** (2016).
1554 https://doi.org:10.7554/eLife.12813
1555 28 Pang, S. Y. *et al.* LRRK2, GBA and their interaction in the regulation of
1556 autophagy: implications on therapeutics in Parkinson's disease. *Transl*
1557 *Neurodegener* **11**, 5 (2022). https://doi.org:10.1186/s40035-022-00281-6
1558 29 Mestre, T. A. *et al.* Clustering of motor and nonmotor traits in leucine-rich repeat
1559 kinase 2 G2019S Parkinson's disease nonparkinsonian relatives: A multicenter
1560 family study. *Mov Disord* **33**, 960-965 (2018). https://doi.org:10.1002/mds.27272
1561 30 Chang, E. E. S. *et al.* LRRK2 mutant knock-in mouse models: therapeutic
1562 relevance in Parkinson's disease. *Translational Neurodegeneration* **11** (2022).
1563 https://doi.org:10.1186/s40035-022-00285-2
1564 31 Yue, M. *et al.* Progressive dopaminergic alterations and mitochondrial
1565 abnormalities in LRRK2 G2019S knock-in mice. *Neurobiol Dis* **78**, 172-195
1566 (2015). https://doi.org:10.1016/j.nbd.2015.02.031

1567 32 Volta, M. & Melrose, H. LRRK2 mouse models: dissecting the behavior, striatal
1568 neurochemistry and neurophysiology of PD pathogenesis. *Biochem Soc Trans*
1569 **45**, 113-122 (2017). https://doi.org:10.1042/BST20160238
1570 33 Hussein, A., Tielemans, A., Baxter, M. G., Benson, D. L. & Huntley, G. W.
1571 Cognitive deficits and altered cholinergic innervation in young adult male mice
1572 carrying a Parkinson's disease Lrrk2(G2019S) knockin mutation. *Exp Neurol* **355**,
1573 114145 (2022). https://doi.org:10.1016/j.expneurol.2022.114145
1574 34 Kuhlmann, N. & Milnerwood, A. J. A Critical LRRK at the Synapse? The
1575 Neurobiological Function and Pathophysiological Dysfunction of LRRK2. *Front*
1576 *Mol Neurosci* **13**, 153 (2020). https://doi.org:10.3389/fnmol.2020.00153
1577 35 Matikainen-Ankney, B. A. *et al.* Parkinson's Disease-Linked LRRK2-G2019S
1578 Mutation Alters Synaptic Plasticity and Promotes Resilience to Chronic Social
1579 Stress in Young Adulthood. *J Neurosci* **38**, 9700-9711 (2018).
1580 https://doi.org:10.1523/JNEUROSCI.1457-18.2018
1581 36 Matikainen-Ankney, B. A. *et al.* Altered Development of Synapse Structure and
1582 Function in Striatum Caused by Parkinson's Disease-Linked LRRK2-G2019S
1583 Mutation. *J Neurosci* **36**, 7128-7141 (2016).
1584 https://doi.org:10.1523/JNEUROSCI.3314-15.2016
1585 37 Lawal, O., Ulloa Severino, F. P. & Eroglu, C. The role of astrocyte structural
1586 plasticity in regulating neural circuit function and behavior. *Glia* **70**, 1467-1483
1587 (2022). https://doi.org:10.1002/glia.24191

1588 38 Hirrlinger, J. & Nimmerjahn, A. A perspective on astrocyte regulation of neural
1589 circuit function and animal behavior. *Glia* **70**, 1554-1580 (2022).
1590 https://doi.org:10.1002/glia.24168
1591 39 Escartin, C. *et al.* Reactive astrocyte nomenclature, definitions, and future
1592 directions. *Nat Neurosci* **24**, 312-325 (2021). https://doi.org:10.1038/s41593-020-
1593 00783-4
1594 40 Stogsdill, J. A. *et al.* Astrocytic neuroligins control astrocyte morphogenesis and
1595 synaptogenesis. *Nature* **551**, 192-197 (2017).
1596 https://doi.org:10.1038/nature24638
1597 41 Sofroniew, M. V. & Vinters, H. V. Astrocytes: biology and pathology. *Acta*
1598 *Neuropathol* **119**, 7-35 (2010). https://doi.org:10.1007/s00401-009-0619-8
1599 42 Hol, E. M. & Pekny, M. Glial fibrillary acidic protein (GFAP) and the astrocyte
1600 intermediate filament system in diseases of the central nervous system. *Curr*
1601 *Opin Cell Biol* **32**, 121-130 (2015). https://doi.org:10.1016/j.ceb.2015.02.004
1602 43 Longo, F. *et al.* Age-dependent dopamine transporter dysfunction and Serine129
1603 phospho-alpha-synuclein overload in G2019S LRRK2 mice. *Acta Neuropathol*
1604 *Commun* **5**, 22 (2017). https://doi.org:10.1186/s40478-017-0426-8
1605 44 Skelton, P. D., Tokars, V. & Parisiadou, L. LRRK2 at Striatal Synapses: Cell-
1606 Type Specificity and Mechanistic Insights. *Cells* **11** (2022).
1607 https://doi.org:10.3390/cells11010169
1608 45 Fremeau, R. T., Jr. *et al.* The expression of vesicular glutamate transporters
1609 defines two classes of excitatory synapse. *Neuron* **31**, 247-260 (2001).
1610 https://doi.org:10.1016/s0896-6273(01)00344-0

1611 46 Micheva, K. D., Busse, B., Weiler, N. C., O'Rourke, N. & Smith, S. J. Single-
1612 synapse analysis of a diverse synapse population: proteomic imaging methods
1613 and markers. *Neuron* **68**, 639-653 (2010).
1614 https://doi.org:10.1016/j.neuron.2010.09.024
1615 47 Ippolito, D. M. & Eroglu, C. Quantifying synapses: an immunocytochemistry-
1616 based assay to quantify synapse number. *J Vis Exp* (2010).
1617 https://doi.org:10.3791/2270
1618 48 Glasgow, S. D., McPhedrain, R., Madranges, J. F., Kennedy, T. E. & Ruthazer,
1619 E. S. Approaches and Limitations in the Investigation of Synaptic Transmission
1620 and Plasticity. *Front Synaptic Neurosci* **11**, 20 (2019).
1621 https://doi.org:10.3389/fnsyn.2019.00020
1622 49 Matsuzaki, M. *et al.* Dendritic spine geometry is critical for AMPA receptor
1623 expression in hippocampal CA1 pyramidal neurons. *Nat Neurosci* **4**, 1086-1092
1624 (2001). https://doi.org:10.1038/nn736
1625 50 Parisiadou, L. *et al.* Phosphorylation of ezrin/radixin/moesin proteins by LRRK2
1626 promotes the rearrangement of actin cytoskeleton in neuronal morphogenesis. *J*
1627 *Neurosci* **29**, 13971-13980 (2009). https://doi.org:10.1523/JNEUROSCI.3799-
1628 09.2009
1629 51 Jaleel, M. *et al.* LRRK2 phosphorylates moesin at threonine-558: characterization
1630 of how Parkinson's disease mutants affect kinase activity. *Biochem J* **405**, 307-
1631 317 (2007). https://doi.org:10.1042/BJ20070209

1632 52 Zhang, Y. *et al.* An RNA-sequencing transcriptome and splicing database of glia,
1633 neurons, and vascular cells of the cerebral cortex. *J Neurosci* **34**, 11929-11947
1634 (2014). https://doi.org:10.1523/JNEUROSCI.1860-14.2014
1635 53 Zhu, L. *et al.* High turnover of ezrin T567 phosphorylation: conformation, activity,
1636 and cellular function. *Am J Physiol Cell Physiol* **293**, C874-884 (2007).
1637 https://doi.org:10.1152/ajpcell.00111.2007
1638 54 Gautreau, A., Louvard, D. & Arpin, M. Morphogenic effects of ezrin require a
1639 phosphorylation-induced transition from oligomers to monomers at the plasma
1640 membrane. *J Cell Biol* **150**, 193-203 (2000). https://doi.org:10.1083/jcb.150.1.193
1641 55 Ito, G. *et al.* Phos-tag analysis of Rab10 phosphorylation by LRRK2: a powerful
1642 assay for assessing kinase function and inhibitors. *Biochem J* **473**, 2671-2685
1643 (2016). https://doi.org:10.1042/BCJ20160557
1644 56 Chua, C. E. L. & Tang, B. L. Rab 10-a traffic controller in multiple cellular
1645 pathways and locations. *J Cell Physiol* **233**, 6483-6494 (2018).
1646 https://doi.org:10.1002/jcp.26503
1647 57 Chaboub, L. S. & Deneen, B. Developmental origins of astrocyte heterogeneity:
1648 the final frontier of CNS development. *Dev Neurosci* **34**, 379-388 (2012).
1649 https://doi.org:10.1159/000343723
1650 58 Molofsky, A. V. *et al.* Astrocytes and disease: a neurodevelopmental perspective.
1651 *Genes Dev* **26**, 891-907 (2012). https://doi.org:10.1101/gad.188326.112
1652 59 Lavialle, M. *et al.* Structural plasticity of perisynaptic astrocyte processes involves
1653 ezrin and metabotropic glutamate receptors. *Proc Natl Acad Sci U S A* **108**,
1654 12915-12919 (2011). https://doi.org:10.1073/pnas.1100957108

1655 60 Endo, F. *et al.* Molecular basis of astrocyte diversity and morphology across the
1656 CNS in health and disease. *Science* **378**, eadc9020 (2022).
1657 https://doi.org:10.1126/science.adc9020
1658 61 Kruyer, A., Scofield, M. D., Wood, D., Reissner, K. J. & Kalivas, P. W. Heroin
1659 Cue-Evoked Astrocytic Structural Plasticity at Nucleus Accumbens Synapses
1660 Inhibits Heroin Seeking. *Biol Psychiatry* **86**, 811-819 (2019).
1661 https://doi.org:10.1016/j.biopsych.2019.06.026
1662 62 Soto, J. S. *et al.* Astrocyte-neuron subproteomes and obsessive-compulsive
1663 disorder mechanisms. *Nature* (2023). https://doi.org:10.1038/s41586-023-05927-
1664 7
1665 63 Fievet, B. T. *et al.* Phosphoinositide binding and phosphorylation act sequentially
1666 in the activation mechanism of ezrin. *J Cell Biol* **164**, 653-659 (2004).
1667 https://doi.org:10.1083/jcb.200307032
1668 64 Yin, L. M. & Schnoor, M. Modulation of membrane-cytoskeleton interactions:
1669 ezrin as key player. *Trends Cell Biol* **32**, 94-97 (2022).
1670 https://doi.org:10.1016/j.tcb.2021.09.005
1671 65 Heiska, L. *et al.* Association of ezrin with intercellular adhesion molecule-1 and -2
1672 (ICAM-1 and ICAM-2). Regulation by phosphatidylinositol 4, 5-bisphosphate. *J*
1673 *Biol Chem* **273**, 21893-21900 (1998). https://doi.org:10.1074/jbc.273.34.21893
1674 66 Zaman, R. *et al.* Effector-mediated ERM activation locally inhibits RhoA activity to
1675 shape the apical cell domain. *J Cell Biol* **220** (2021).
1676 https://doi.org:10.1083/jcb.202007146

1677 67 Tsai, F. C. *et al.* Ezrin enrichment on curved membranes requires a specific
1678 conformation or interaction with a curvature-sensitive partner. *Elife* **7** (2018).
1679 https://doi.org:10.7554/eLife.37262
1680 68 Matsui, T. *et al.* Rho-kinase phosphorylates COOH-terminal threonines of
1681 ezrin/radixin/moesin (ERM) proteins and regulates their head-to-tail association.
1682 *J Cell Biol* **140**, 647-657 (1998). https://doi.org:10.1083/jcb.140.3.647
1683 69 Shani, V. *et al.* Physiological and pathological roles of LRRK2 in the nuclear
1684 envelope integrity. *Hum Mol Genet* **28**, 3982-3996 (2019).
1685 https://doi.org:10.1093/hmg/ddz245
1686 70 Heaton, G. R. *et al.* Sequential screening nominates the Parkinson's disease
1687 associated kinase LRRK2 as a regulator of Clathrin-mediated endocytosis.
1688 *Neurobiol Dis* **141**, 104948 (2020). https://doi.org:10.1016/j.nbd.2020.104948
1689 71 Soto, J. S. *et al.* Astrocyte-neuron subproteomes and obsessive-compulsive
1690 disorder mechanisms. *Nature* **616**, 764-773 (2023).
1691 https://doi.org:10.1038/s41586-023-05927-7
1692 72 Plowey, E. D., Cherra, S. J., 3rd, Liu, Y. J. & Chu, C. T. Role of autophagy in
1693 G2019S-LRRK2-associated neurite shortening in differentiated SH-SY5Y cells. *J*
1694 *Neurochem* **105**, 1048-1056 (2008). https://doi.org:10.1111/j.1471-
1695 4159.2008.05217.x
1696 73 Mizushima, N. *et al.* A protein conjugation system essential for autophagy.
1697 *Nature* **395**, 395-398 (1998). https://doi.org:10.1038/26506

1698 74 Collier, J. J. *et al.* Developmental Consequences of Defective ATG7-Mediated
1699 Autophagy in Humans. *N Engl J Med* **384**, 2406-2417 (2021).
1700 https://doi.org:10.1056/NEJMoa1915722
1701 75 Evans, R. *et al.* Protein complex prediction with AlphaFold-Multimer. *bioRxiv*,
1702 2021.2010.2004.463034 (2022). https://doi.org:10.1101/2021.10.04.463034
1703 76 Kaiser, S. E. *et al.* Structures of Atg7-Atg3 and Atg7-Atg10 reveal noncanonical
1704 mechanisms of E2 recruitment by the autophagy E1. *Autophagy* **9**, 778-780
1705 (2013). https://doi.org:10.4161/auto.23644
1706 77 Pelaseyed, T. *et al.* Ezrin activation by LOK phosphorylation involves a PIP(2)-
1707 dependent wedge mechanism. *Elife* **6** (2017). https://doi.org:10.7554/eLife.22759
1708 78 Bravo-San Pedro, J. M. *et al.* The LRRK2 G2019S mutant exacerbates basal
1709 autophagy through activation of the MEK/ERK pathway. *Cell Mol Life Sci* **70**,
1710 121-136 (2013). https://doi.org:10.1007/s00018-012-1061-y
1711 79 Arakawa, S., Honda, S., Yamaguchi, H. & Shimizu, S. Molecular mechanisms
1712 and physiological roles of Atg5/Atg7-independent alternative autophagy. *Proc*
1713 *Jpn Acad Ser B Phys Biol Sci* **93**, 378-385 (2017).
1714 https://doi.org:10.2183/pjab.93.023
1715 80 Nishida, Y. *et al.* Discovery of Atg5/Atg7-independent alternative
1716 macroautophagy. *Nature* **461**, 654-658 (2009).
1717 https://doi.org:10.1038/nature08455
1718 81 Durgan, J. *et al.* Non-canonical autophagy drives alternative ATG8 conjugation to
1719 phosphatidylserine. *Mol Cell* **81**, 2031-2040 e2038 (2021).
1720 https://doi.org:10.1016/j.molcel.2021.03.020

1721 82 Durgan, J. & Florey, O. A new flavor of cellular Atg8-family protein lipidation -
1722 alternative conjugation to phosphatidylserine during CASM. *Autophagy* **17**, 2642-
1723 2644 (2021). https://doi.org:10.1080/15548627.2021.1947730
1724 83 Giamundo, G. *et al.* Ezrin defines TSC1 activation at endosomal compartments
1725 through EGFR-AKT signaling. *bioRxiv*, 2024.2005.2003.592332 (2024).
1726 https://doi.org:10.1101/2024.05.03.592332
1727 84 Broadhead, M. J. *et al.* Selective vulnerability of tripartite synapses in
1728 amyotrophic lateral sclerosis. *Acta Neuropathol* **143**, 471-486 (2022).
1729 https://doi.org:10.1007/s00401-022-02412-9
1730 85 Hussein, A. *et al.* Non-Motor Symptoms of Parkinson's Disease: The
1731 Neurobiology of Early Psychiatric and Cognitive Dysfunction. *Neuroscientist*,
1732 10738584211011979 (2021). https://doi.org:10.1177/10738584211011979
1733 86 Guevara, C. A. *et al.* LRRK2 mutation alters behavioral, synaptic, and
1734 nonsynaptic adaptations to acute social stress. *J Neurophysiol* **123**, 2382-2389
1735 (2020). https://doi.org:10.1152/jn.00137.2020
1736 87 Shenhav, A., Botvinick, M. M. & Cohen, J. D. The expected value of control: an
1737 integrative theory of anterior cingulate cortex function. *Neuron* **79**, 217-240
1738 (2013). https://doi.org:10.1016/j.neuron.2013.07.007
1739 88 Tervo, D. G. R. *et al.* The anterior cingulate cortex directs exploration of
1740 alternative strategies. *Neuron* **109**, 1876-1887 e1876 (2021).
1741 https://doi.org:10.1016/j.neuron.2021.03.028

1742 89 Lanjakornsiripan, D. *et al.* Layer-specific morphological and molecular
1743 differences in neocortical astrocytes and their dependence on neuronal layers.
1744 *Nat Commun* **9**, 1623 (2018). https://doi.org:10.1038/s41467-018-03940-3
1745 90 Bayraktar, O. A. *et al.* Astrocyte layers in the mammalian cerebral cortex
1746 revealed by a single-cell in situ transcriptomic map. *Nat Neurosci* **23**, 500-509
1747 (2020). https://doi.org:10.1038/s41593-020-0602-1
1748 91 Savage, J. T. *et al.* SynBot: An open-source image analysis software for
1749 automated quantification of synapses. *bioRxiv* (2024).
1750 https://doi.org:10.1101/2023.06.26.546578
1751 92 Kim, Y. G., Shin, J. J. & Kim, S. J. Minhee Analysis Package: an integrated
1752 software package for detection and management of spontaneous synaptic
1753 events. *Mol Brain* **14**, 138 (2021). https://doi.org:10.1186/s13041-021-00847-x
1754 93 Tan, C. X. *et al.* delta-Catenin controls astrocyte morphogenesis via layer-
1755 specific astrocyte-neuron cadherin interactions. *J Cell Biol* **222** (2023).
1756 https://doi.org:10.1083/jcb.202303138
1757 94 Moffat, J. *et al.* A lentiviral RNAi library for human and mouse genes applied to
1758 an arrayed viral high-content screen. *Cell* **124**, 1283-1298 (2006).
1759 https://doi.org:10.1016/j.cell.2006.01.040
1760 95 Chih, B., Gollan, L. & Scheiffele, P. Alternative splicing controls selective trans-
1761 synaptic interactions of the neuroligin-neurexin complex. *Neuron* **51**, 171-178
1762 (2006). https://doi.org:10.1016/j.neuron.2006.06.005

1763 96 Chen, F. & LoTurco, J. A method for stable transgenesis of radial glia lineage in
1764 rat neocortex by piggyBac mediated transposition. *J Neurosci Methods* **207**, 172-
1765 180 (2012). https://doi.org:10.1016/j.jneumeth.2012.03.016
1766 97 O'Neil, S. D. *et al.* Action potential-coupled Rho GTPase signaling drives
1767 presynaptic plasticity. *Elife* **10** (2021). https://doi.org:10.7554/eLife.63756
1768 98 Ferreira, T. A. *et al.* Neuronal morphometry directly from bitmap images. *Nat*
1769 *Methods* **11**, 982-984 (2014). https://doi.org:10.1038/nmeth.3125
1770 99 Uezu, A. *et al.* Identification of an elaborate complex mediating postsynaptic
1771 inhibition. *Science* **353**, 1123-1129 (2016).
1772 https://doi.org:10.1126/science.aag0821
1773 100 Kuriata, A. *et al.* CABS-flex 2.0: a web server for fast simulations of flexibility of
1774 protein structures. *Nucleic Acids Res* **46**, W338-W343 (2018).
1775 https://doi.org:10.1093/nar/gky356
1776 101 Takano, T. *et al.* Chemico-genetic discovery of astrocytic control of inhibition in
1777 vivo. *Nature* **588**, 296-302 (2020). https://doi.org:10.1038/s41586-020-2926-0
1778 102 Risher, W. C. *et al.* Thrombospondin receptor alpha2delta-1 promotes
1779 synaptogenesis and spinogenesis via postsynaptic Rac1. *J Cell Biol* **217**, 3747-
1780 3765 (2018). https://doi.org:10.1083/jcb.201802057

1781

Figure 1

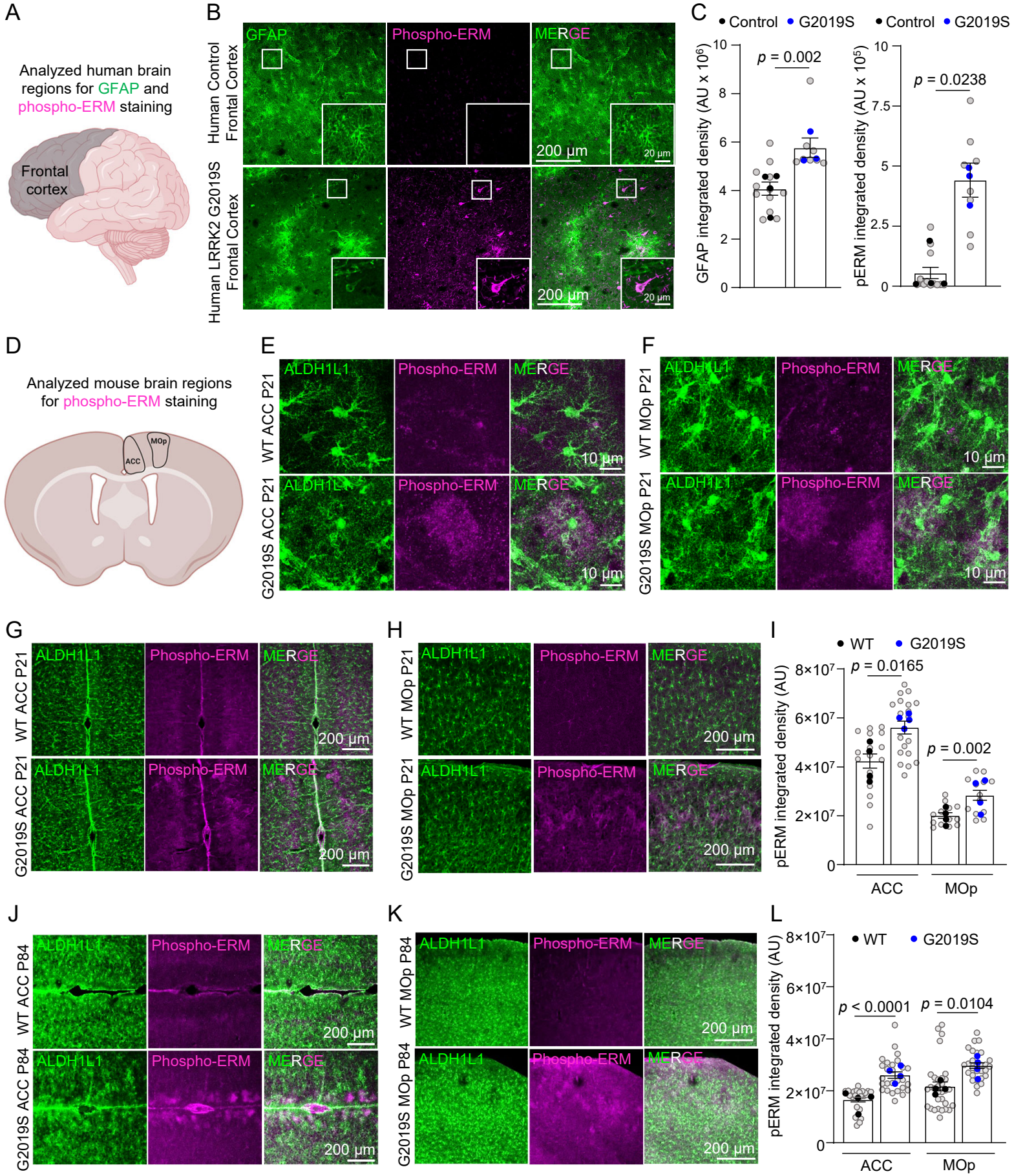
A
Analyzed human brain regions for GFAP and phospho-ERM staining
Frontal cortex
B
Human Control Frontal Cortex
Human LRRK2 G2019S Frontal Cortex
GFAP
Phospho-ERM
MERGE
200 µm
20 µm
C
Control
G2019S
GFAP integrated density (AU x 10^6)
p = 0.002
pERM integrated density (AU x 10^5)
p = 0.0238
D
Analyzed mouse brain regions for phospho-ERM staining
ACC
MOp
E
WT ACC P21
G2019S ACC P21
ALDH1L1
Phospho-ERM
MERGE
10 µm
F
WT MOp P21
G2019S MOp P21
G
WT ACC P21
G2019S ACC P21
200 µm
H
WT MOp P21
G2019S MOp P21
I
WT
G2019S
pERM integrated density (AU)
p = 0.0165
p = 0.002
ACC
MOp
J
WT ACC P84
G2019S ACC P84
K
WT MOp P84
G2019S MOp P84
L
p < 0.0001
p = 0.0104

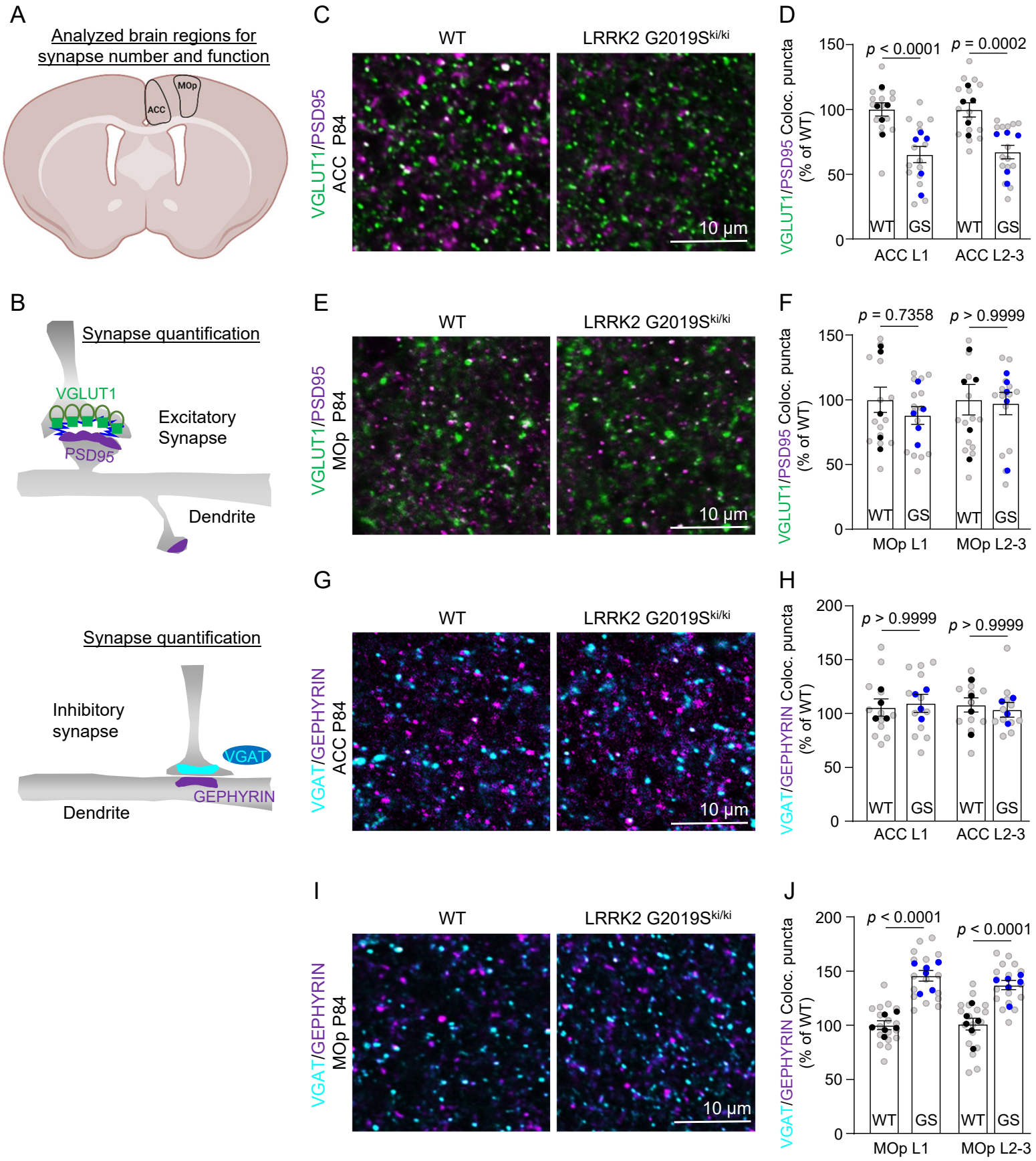
A
Analyzed brain regions for synapse number and function
MOp
ACC
B
Synapse quantification
VGLUT1
Excitatory Synapse
PSD95
Dendrite
Synapse quantification
Inhibitory synapse
VGAT
GEPHYRIN
Dendrite
C
WT
LRRK2 G2019S ki/ki
VGLUT1/PSD95 ACC P84
10 µm
D
VGLUT1/PSD95 Coloc. puncta (% of WT)
p < 0.0001
p = 0.0002
WT GS WT GS
ACC L1
ACC L2-3
E
WT
LRRK2 G2019S ki/ki
VGLUT1/PSD95 MOp P84
10 µm
F
p = 0.7358
p > 0.9999
MOp L1
MOp L2-3
G
WT
LRRK2 G2019S ki/ki
VGAT/GEPHYRIN ACC P84
10 µm
H
VGAT/GEPHYRIN Coloc. puncta (% of WT)
p > 0.9999
p > 0.9999
ACC L1
ACC L2-3
I
WT
LRRK2 G2019S ki/ki
VGAT/GEPHYRIN MOp P84
10 µm
J
p < 0.0001
p < 0.0001
MOp L1
MOp L2-3

Figure 3

Wang et al.,

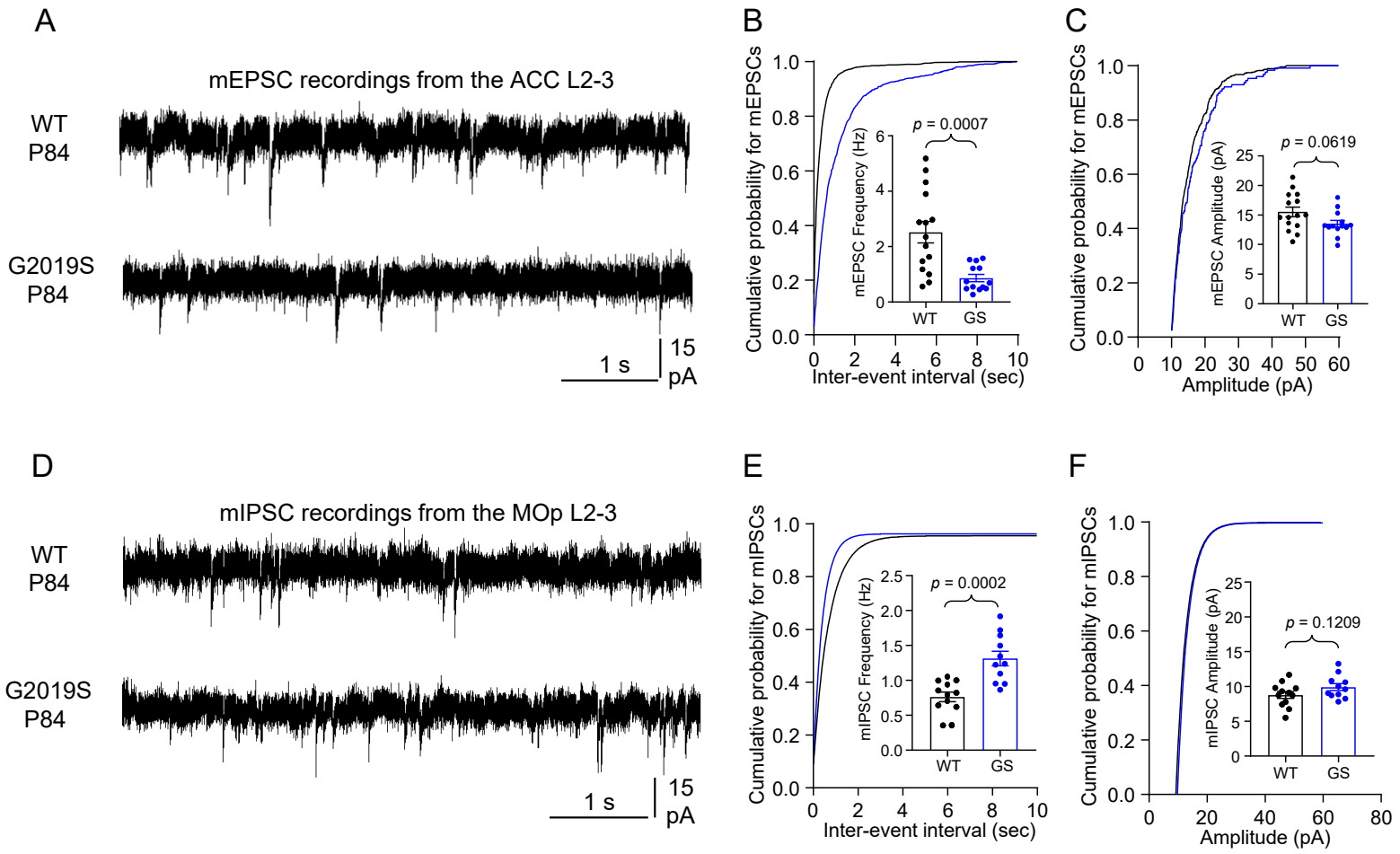

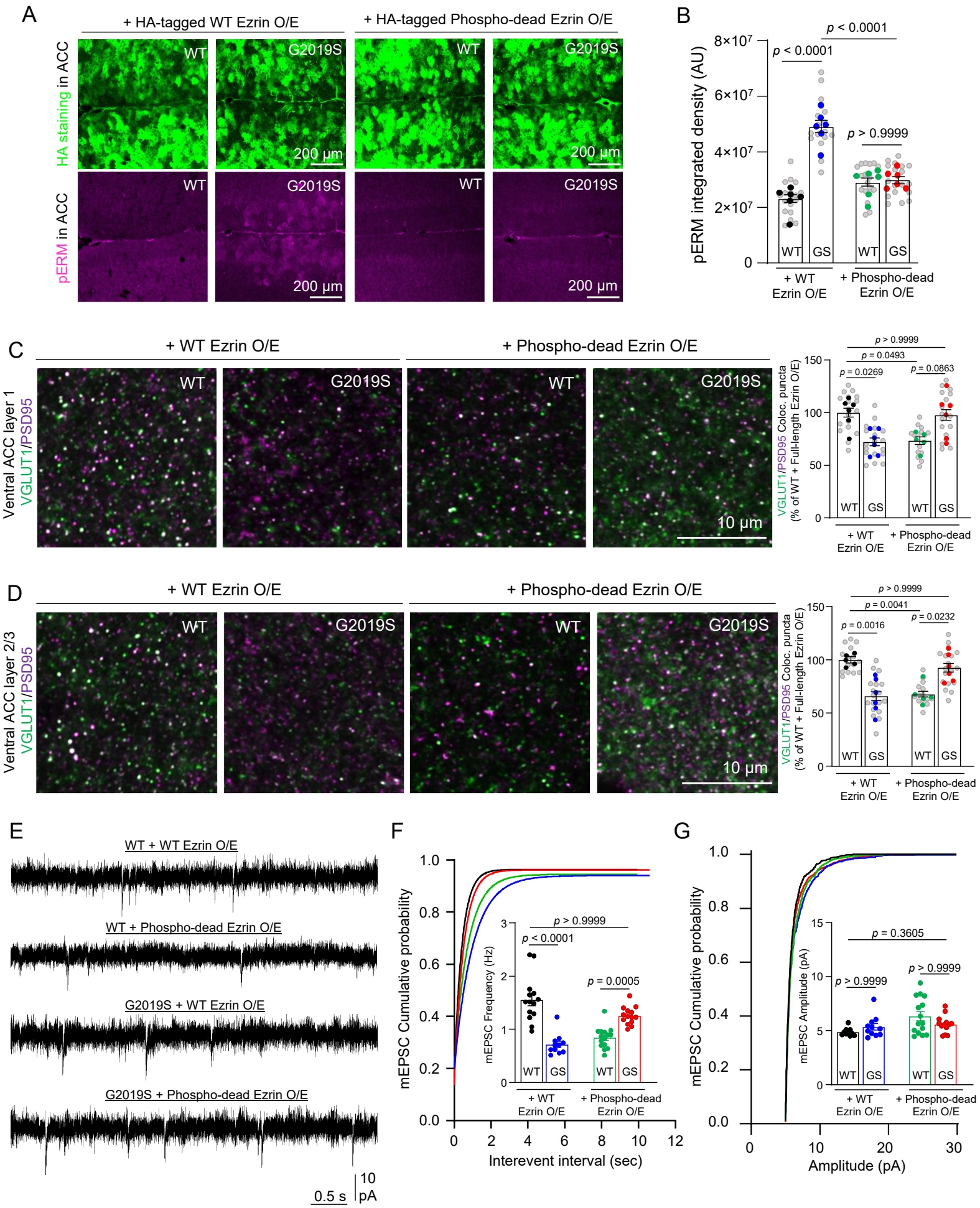
A
+ HA-tagged WT Ezrin O/E
+ HA-tagged Phospho-dead Ezrin O/E
HA staining in ACC
pERM in ACC
WT
G2019S
200 µm
B
pERM integrated density (AU)
p < 0.0001
p > 0.9999
+ WT Ezrin O/E
+ Phospho-dead Ezrin O/E
C
+ WT Ezrin O/E
+ Phospho-dead Ezrin O/E
Ventral ACC layer 1
VGLUT1/PSD95
10 µm
VGLUT1/PSD95 Coloc. puncta (% of WT + Full-length Ezrin O/E)
p = 0.0269
p = 0.0493
p = 0.0863
D
Ventral ACC layer 2/3
p = 0.0016
p = 0.0041
p = 0.0232
E
WT + WT Ezrin O/E
WT + Phospho-dead Ezrin O/E
G2019S + WT Ezrin O/E
G2019S + Phospho-dead Ezrin O/E
0.5 s
10 pA
F
mEPSC Cumulative probability
Interevent interval (sec)
mEPSC Frequency (Hz)
p = 0.0005
G
Amplitude (pA)
mEPSC Amplitude (pA)
p = 0.3605

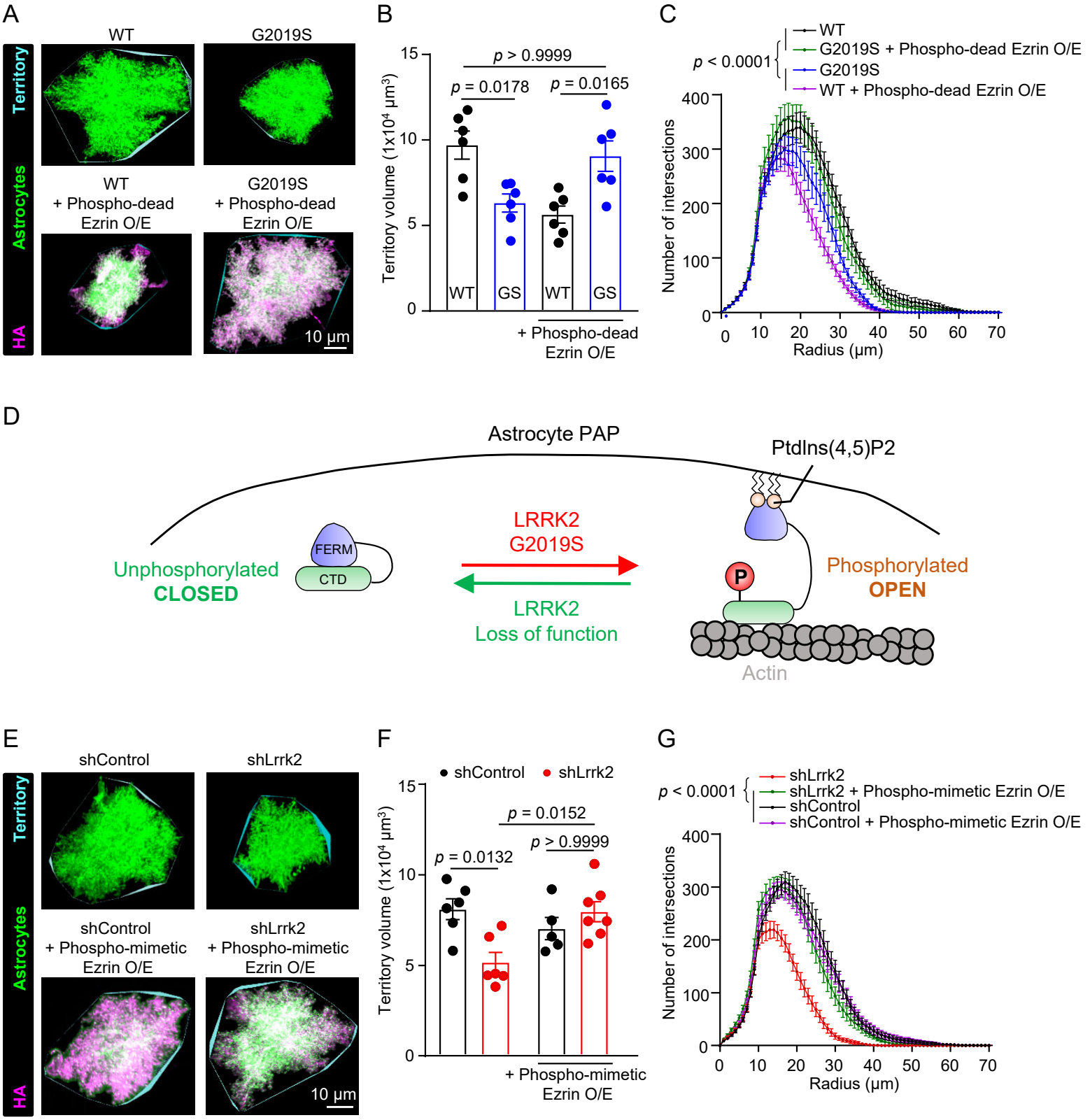
A
WT
G2019S
Territory
Astrocytes
HA
WT
+ Phospho-dead
Ezrin O/E
G2019S
+ Phospho-dead
Ezrin O/E
10 µm
B
Territory volume (1x10⁴ µm³)
p > 0.9999
p = 0.0178
p = 0.0165
WT
GS
WT
GS
+ Phospho-dead
Ezrin O/E
C
p < 0.0001
WT
G2019S + Phospho-dead Ezrin O/E
G2019S
WT + Phospho-dead Ezrin O/E
Number of intersections
Radius (µm)
D
Astrocyte PAP
PtdIns(4,5)P2
Unphosphorylated
CLOSED
FERM
CTD
LRRK2
G2019S
LRRK2
Loss of function
P
Phosphorylated
OPEN
Actin
E
shControl
shLrrk2
Territory
Astrocytes
HA
shControl
+ Phospho-mimetic
Ezrin O/E
shLrrk2
+ Phospho-mimetic
Ezrin O/E
10 µm
F
shControl
shLrrk2
Territory volume (1x10⁴ µm³)
p = 0.0152
p = 0.0132
p > 0.9999
+ Phospho-mimetic
Ezrin O/E
G
p < 0.0001
shLrrk2
shLrrk2 + Phospho-mimetic Ezrin O/E
shControl
shControl + Phospho-mimetic Ezrin O/E
Number of intersections
Radius (µm)

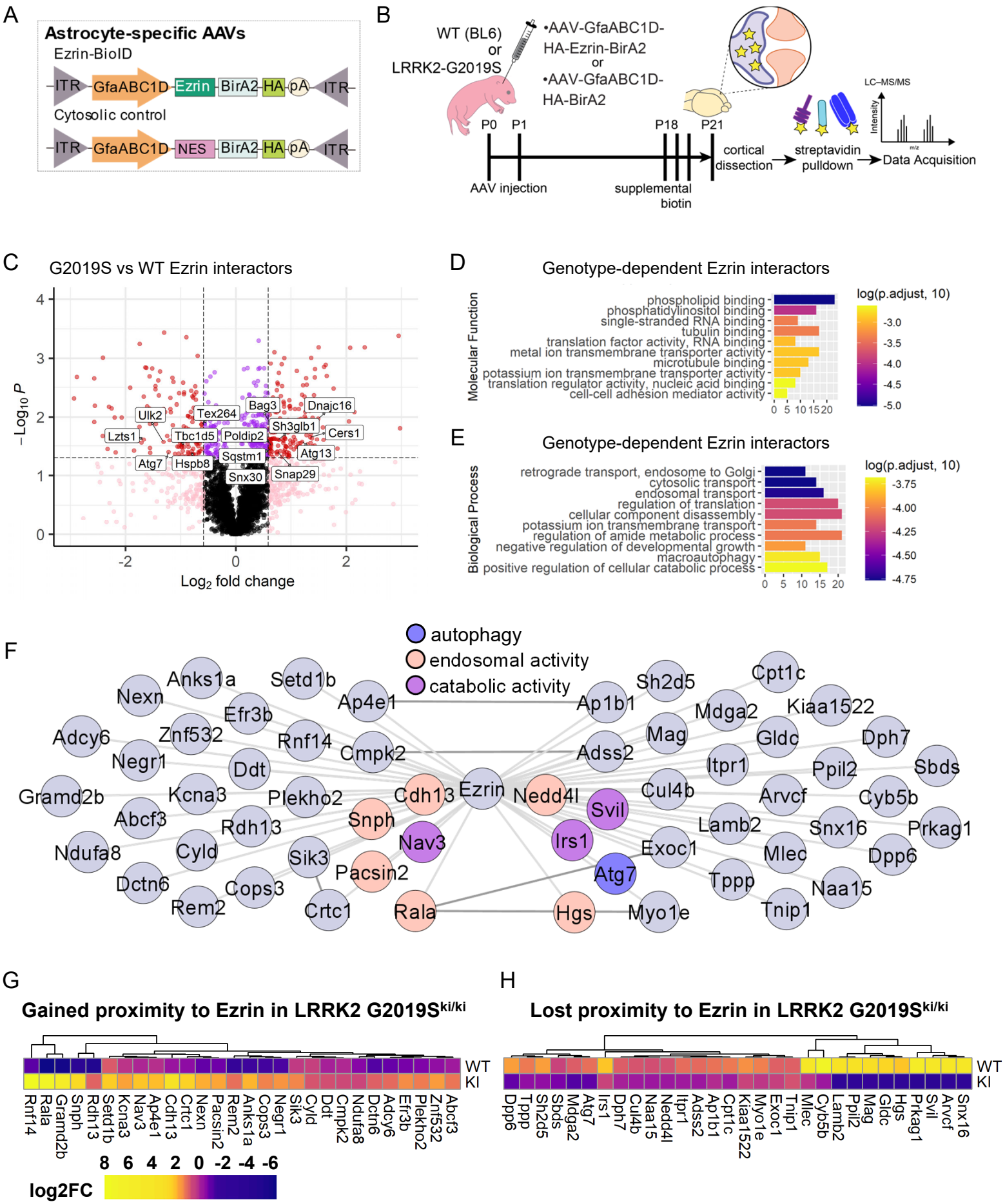
A
Astrocyte-specific AAVs
Ezrin-BioID
ITR GfaABC1D Ezrin BirA2 HA pA ITR
Cytosolic control
ITR GfaABC1D NES BirA2 HA pA ITR
B
WT (BL6) or LRRK2-G2019S
•AAV-GfaABC1D-HA-Ezrin-BirA2 or •AAV-GfaABC1D-HA-BirA2
P0 P1 P18 P21
AAV injection
supplemental biotin
cortical dissection
streptavidin pulldown
LC–MS/MS
Data Acquisition
C
G2019S vs WT Ezrin interactors
−Log10 P
Log2 fold change
Ulk2 Tex264 Bag3 Dnajc16 Lzts1 Tbc1d5 Poldip2 Sh3glb1 Cers1 Atg7 Hspb8 Sqstm1 Atg13 Snx30 Snap29
D
Genotype-dependent Ezrin interactors
Molecular Function
phospholipid binding
phosphatidylinositol binding
single-stranded RNA binding
tubulin binding
translation factor activity, RNA binding
metal ion transmembrane transporter activity
microtubule binding
potassium ion transmembrane transporter activity
translation regulator activity, nucleic acid binding
cell-cell adhesion mediator activity
log(p.adjust, 10)
E
Genotype-dependent Ezrin interactors
Biological Process
retrograde transport, endosome to Golgi
cytosolic transport
endosomal transport
regulation of translation
cellular component disassembly
potassium ion transmembrane transport
regulation of amide metabolic process
negative regulation of developmental growth
macroautophagy
positive regulation of cellular catabolic process
log(p.adjust, 10)
F
autophagy
endosomal activity
catabolic activity
Ezrin
Anks1a Setd1b Nexn Efr3b Ap4e1 Adcy6 Znf532 Rnf14 Negr1 Ddt Cmpk2 Gramd2b Kcna3 Plekho2 Abcf3 Rdh13 Cdh13 Snph Ndufa8 Cyld Nav3 Sik3 Pacsin2 Dctn6 Cops3 Rem2 Crtc1 Rala
Ap1b1 Sh2d5 Cpt1c Mdga2 Kiaa1522 Mag Gldc Dph7 Adss2 Itpr1 Ppil2 Sbds Cul4b Arvcf Cyb5b Nedd4l Svil Lamb2 Snx16 Prkag1 Irs1 Exoc1 Mlec Dpp6 Atg7 Tppp Naa15 Hgs Myo1e Tnip1
G
Gained proximity to Ezrin in LRRK2 G2019Ski/ki
WT
KI
Rnf14 Rala Gramd2b Snph Rdh13 Setd1b Kcna3 Nav3 Ap4e1 Cdh13 Crtc1 Nexn Pacsin2 Rem2 Anks1a Cops3 Negr1 Sik3 Cyld Ddt Cmpk2 Ndufa8 Dctn6 Adcy6 Efr3b Plekho2 Znf532 Abcf3
8 6 4 2 0 -2 -4 -6
log2FC
H
Lost proximity to Ezrin in LRRK2 G2019Ski/ki
WT
KI
Dpp6 Tppp Sh2d5 Sbds Mdga2 Atg7 Irs1 Dph7 Cul4b Naa15 Nedd4l Itpr1 Adss2 Ap1b1 Cpt1c Kiaa1522 Myo1e Exoc1 Tnip1 Mlec Cyb5b Lamb2 Ppil2 Mag Gldc Hgs Prkag1 Svil Arvcf Snx16

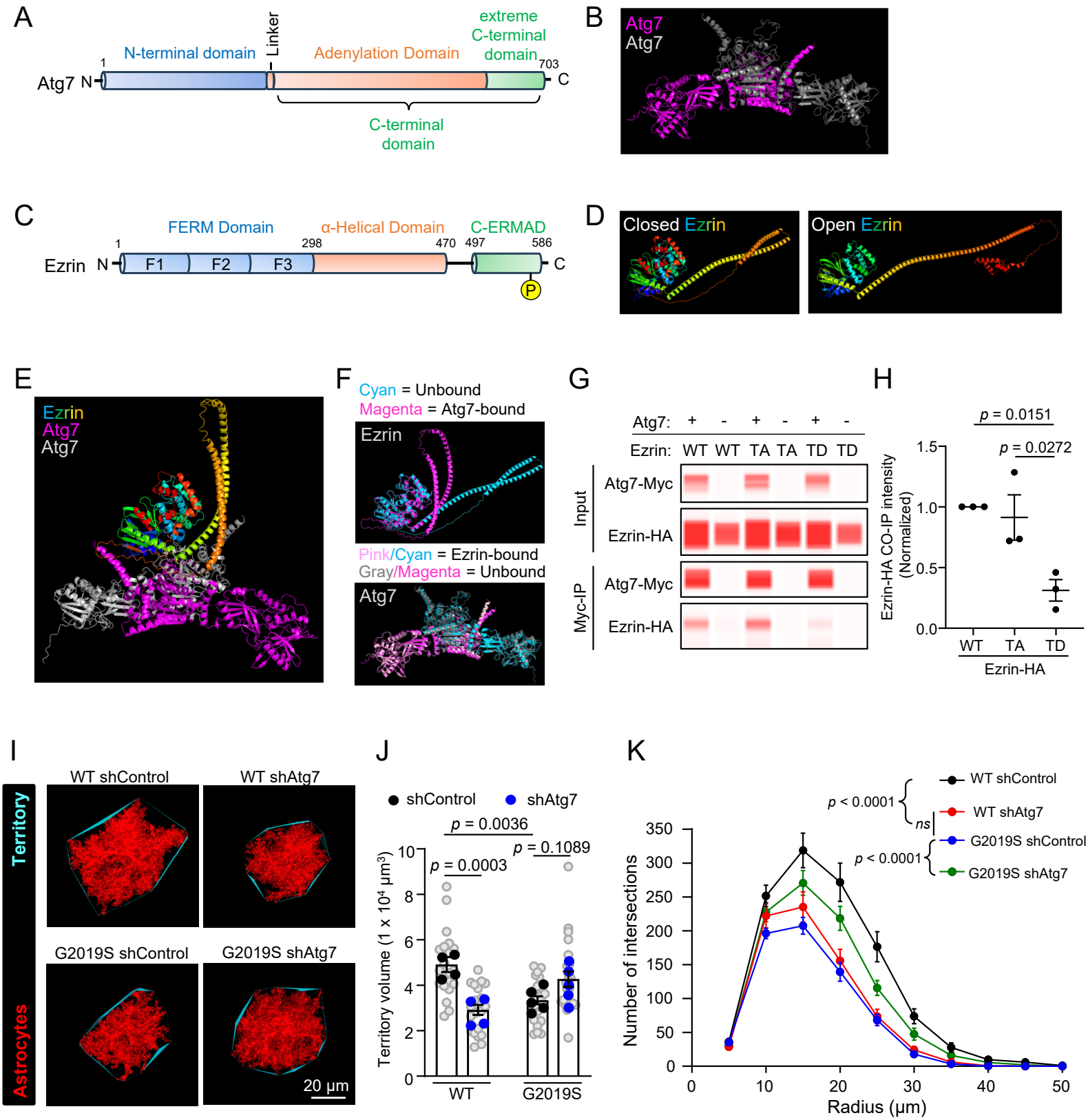
A
Atg7 N
1
N-terminal domain
Linker
Adenylation Domain
extreme C-terminal domain
703
C
C-terminal domain
B
Atg7
Atg7
C
Ezrin N
FERM Domain
α-Helical Domain
C-ERMAD
1
298
470
497
586
F1
F2
F3
P
C
D
Closed Ezrin
Open Ezrin
E
Ezrin
Atg7
Atg7
F
Cyan = Unbound
Magenta = Atg7-bound
Ezrin
Pink/Cyan = Ezrin-bound
Gray/Magenta = Unbound
Atg7
G
Atg7: + - + - + -
Ezrin: WT WT TA TA TD TD
Input
Atg7-Myc
Ezrin-HA
Myc-IP
Atg7-Myc
Ezrin-HA
H
p = 0.0151
p = 0.0272
Ezrin-HA CO-IP intensity (Normalized)
1.5
1.0
0.5
0.0
WT TA TD
Ezrin-HA
I
Territory
Astrocytes
WT shControl
WT shAtg7
G2019S shControl
G2019S shAtg7
20 µm
J
shControl
shAtg7
p = 0.0036
p = 0.0003
p = 0.1089
Territory volume (1 x 10⁴ µm³)
10
8
6
4
2
0
WT
G2019S
K
WT shControl
WT shAtg7
G2019S shControl
G2019S shAtg7
p < 0.0001
ns
p < 0.0001
Number of intersections
350
300
250
200
150
100
50
0
0 10 20 30 40 50
Radius (µm)